The Astrophysical Journal, 813:45 (26pp), 2015 November 1 doi:10.1088/0004-637X/813/1/45

RADIO JET FEEDBACK AND STAR FORMATION IN HEAVILY OBSCURED, HYPERLUMINOUS QUASARS AT REDSHIFTS ∼ 0.5–3. I. ALMA OBSERVATIONS

Carol J. Lonsdale[1], M. Lacy[1,17], A. E. Kimball[1,2,17], A. Blain[3], M. Whittle[4], B. Wilkes[5], D. Stern[6], J. Condon[1], M. Kim[7,8,9], R. J. Assef[10,17], C.-W. Tsai[6], A. Efstathiou[11], S. Jones[3], P. Eisenhardt[6], C. Bridge[12], J. Wu[13], Colin J. Lonsdale[14], K. Jones[4], T. Jarrett[15], and R. Smith[16]

[1] National Radio Astronomy Observatory, Charlottesville, VA 22903, USA; clonsdal@nrao.edu
[2] CSIRO Astronomy and Space Science, Australia Telescope National Facility, P.O. Box 76, Epping, NSW 1710, Australia
[3] Department of Physics & Astronomy, University of Leicester, University Road, Leicester LE1 7RH, UK
[4] Department of Astronomy, University of Virginia, Charlottesville, VA 22903, USA
[5] Harvard-Smithsonian Center for Astrophysics, Cambridge, MA 02138, USA
[6] Jet Propulsion Laboratory, California Institute of Technology, Pasadena, CA 91109, USA
[7] The Observatories of the Carnegie Institution for Science, 813 Santa Barbara Street, Pasadena, CA 91101, USA
[8] Korea Astronomy and Space Science Institute, Daejeon 305-348, Korea
[9] KASI-Carnegie Fellow, The Observatories of the Carnegie Institution for Science, Pasadena, CA 91101, USA
[10] Núcleo de Astronomía de la Facultad de Ingeniería, Universidad Diego Portales, Av. Ejército Libertador 441, Santiago, Chile; NASA Postdoctoral Program (NPP)
[11] School of Sciences, European University Cyprus, Diogenes Street, Engomi, 1516 Nicosia, Cyprus
[12] California Institute of Technology, 249-17, Pasadena, CA 91125, USA
[13] Division of Astronomy & Astrophysics, University of California, Los Angeles, Physics and Astronomy Building, 430 Portola Plaza, Los Angeles, CA 90095-1547, USA
[14] Massachusetts Institute of Technology, Haystack Observatory, Westford, MA 01886, USA
[15] Astronomy Department, University of Cape Town, Cape Town, South Africa
[16] Department of Physics, 3141 Chestnut Street, Drexel University, Philadelphia, PA 19104, USA
Received 2015 April 7; accepted 2015 August 28; published 2015 October 27

ABSTRACT

We present Atacama Large Millimeter/submillimeter Array (ALMA) 870 μm (345 GHz) data for 49 high-redshift ($0.47 < z < 2.85$), luminous ($11.7 < \log(L_{\rm bol}/L_{\odot}) < 14.2$) radio-powerful active galactic nuclei (AGNs), obtained to constrain cool dust emission from starbursts concurrent with highly obscured radiative-mode black hole (BH) accretion in massive galaxies that possess a small radio jet. The sample was selected from the *Wide-field Infrared Survey Explorer* with extremely steep (red) mid-infrared colors and with compact radio emission from NVSS/FIRST. Twenty-six sources are detected at 870 μm, and we find that the sample has large mid- to far-infrared luminosity ratios, consistent with a dominant and highly obscured quasar. The rest-frame 3 GHz radio powers are $24.7 < \log(P_{3.0\,\rm GHz}/\rm W\ Hz^{-1}) < 27.3$, and all sources are radio-intermediate or radio-loud. BH mass estimates are $7.7 < \log(M_{\rm BH}/M_{\odot}) < 10.2$. The rest-frame 1–5 μm spectral energy distributions are very similar to the "Hot DOGs" (hot dust-obscured galaxies), and steeper (redder) than almost any other known extragalactic sources. ISM masses estimated for the ALMA-detected sources are $9.9 < \log(M_{\rm ISM}/M_{\odot}) < 11.75$ assuming a dust temperature of 30 K. The cool dust emission is consistent with star formation rates reaching several thousand $M_{\odot}$ $\rm yr^{-1}$, depending on the assumed dust temperature, but we cannot rule out the alternative that the AGN powers all the emission in some cases. Our best constrained source has radiative transfer solutions with approximately equal contributions from an obscured AGN and a young (10–15 Myr) compact starburst.

Key words: galaxies: active – galaxies: evolution – galaxies: jets – quasars: general – radio continuum: galaxies – submillimeter: galaxies

1. INTRODUCTION

Central questions concerning coeval galaxy and supermassive black hole (SMBH) evolution include the relative timescales and mechanisms for stellar mass and black hole (BH) mass building including the roles and duty cycles of (a) secular versus merger-triggered mechanisms for driving material into the central regions; (b) "radiative-mode" versus "jet-mode" BH accretion modes and rates; and (c) "quasar-mode" versus "radio-mode" feedback mechanisms, all as a function of epoch, galaxy mass, and galaxy environment. Jet-mode active galactic nuclei (AGNs) are low-excitation systems in which the AGN is powered by advection-dominated accretion flows onto the BH with a low accretion rate, as recently reviewed by Heckman & Best (2014). AGNs in jet mode are expected to have low radiative emission and to be energetically dominated by the jet kinetic outflow. Jet-mode radio AGNs are thought to be highly effective in maintaining galaxies free of new gas and star formation via "radio-mode" kinetic feedback, i.e. jet inflation of bubbles in the surrounding hot intergalactic gas (Croton 2006; Cattaneo & Teyssier 2007; Fabian 2010). Radiative-mode, or "quasar-mode," AGNs have higher accretion rates from a thin accretion disk whose radiation powers the narrow- and broad-line regions, and which is fed through a surrounding dusty torus or "torus-like" structure. Quasar-mode accretion has a lower duty cycle than jet-mode, occurring when large amounts of material are available for accretion onto the SMBH. Quasar-mode AGNs are capable of powering efficient feedback into the host galaxy via thermal winds from the accretion disk, disrupting star formation and ejecting gas.

Powerful jets are also found in ∼10% of radiatively efficient AGNs, the radio-loud QSOs (also known as broad-line radio

[17] Visiting Astronomer, Cerro Tololo Inter-American Observatory. CTIO is operated by AURA, Inc., under contract to the National Science Foundation.

galaxies, BLRGs, and high excitation radio galaxies, HERGs), and therefore jets may also contribute to feedback activity in quasar-mode AGNs (Holt et al. 2008; Nesvadba et al. 2008). It is often assumed that the high-radio-power Fanaroff–Riley type II (FRII) jets are too collimated to impact the ISM within host galaxies (De Young 2010). However, high-resolution hydrodynamic models by Wagner & Bicknell (2011) and Wagner et al. (2012, 2013) have demonstrated that the impact of powerful jets on the ISM within the central regions of AGN host galaxies is highly dependent on the density, the filling factor, and the average size of the cool clouds within the ISM. High porosity leads to the inflation of a cocoon by the overpressured jet, leading to a quasispherical bubble being driven into the ISM. Wagner & Bicknell (2011) and Wagner et al. (2012) find that jets of moderate to high power can accelerate dense ISM gas from a hundred to several thousand $\mathrm{km\,s^{-1}}$, with wide-angle flows, within 10–100 Myr.

Best & Heckman (2012) and Best et al. (2014) have shown that the two populations of radio AGNs, quasar-mode (or radiative-mode) and radio-mode (or jet-mode), are both found across all radio luminosities, and that the radiative-mode radio AGNs show much stronger evolution with cosmic time than jet-mode radio AGN, with an order-of-magnitude increase in space density out to $z \sim 1$. This evolution in space density is similar to that of the star formation rate (SFR) density and the quasar luminosity function, consistent with the scenario that the radiative-mode AGNs are controlled by episodic cold gas supply.

Gas flows associated with gas-rich mergers are the likely source of episodic cold gas fueling, important for building galaxies and BHs by triggering both starbursts and AGN activity. Morphological signatures of mergers have been found in a large faction of powerful, $z < 0.7$, radio galaxies (RGs) which display spectroscopic signatures of young stellar populations (Tadhunter et al. 2011), and those with the youngest stellar populations (<0.1 Gyr) show a correlation with mid- to far-infrared and [O III] luminosity, indicating the presence of a radiative-mode AGN. Tadhunter et al. (2011) also find significant complexity in correlations between the triggering or re-triggering of jets, recent star formation, and the merging of the dual nuclei, implying chaotic gas infall histories during merger events, while Dicken et al. (2011) find evidence for the strongest correlation between recent star formation and radio jets for the radio AGNs with the most compact jets. These results support the idea that small (young) radio jets play an important role in the evolution of massive galaxies and SMBHs during merger-driven phases of high accretion rate.

In this series of papers we address the impact of young, moderate to powerful, radio jets from luminous, radiatively efficient, highly obscured, radio AGNs on the disruption of the ISM and star formation in their hosts at redshifts near the peak of galaxy and BH building, $z \sim 1-3$. We also consider the possibility of ISM compression and starburst triggering by jet kinetic energy. By selecting systems with a high mid-infrared (MIR) luminosity we aim to identify radiatively efficient AGNs, and by selecting compact radio sources we favor young radio jets that are confined within the hosts. By selecting AGNs that are very red through the optical–MIR we favor highly obscured systems likely to be in a peak fueling phase.

A nearby example of such a system is the MIR-bright QSO Mrk 231, which has a luminous radiative-mode AGN, two small radio jet systems (2 and 40 pc) (Ulvestad et al. 1999; Lonsdale et al. 2003), and powerful molecular outflows (Fischer et al. 2010; Gonzalez-Alfonso et al. 2014; Aalto et al. 2015; Feruglio et al. 2015). Mrk 231 also shows a bright optical core, indicating a complex nuclear geometry.

1.1. Evidence for Radio Jet Interactions with Molecular Gas

Most early studies of outflows from AGNs targeted the ionized gas, which, because of its much lower mass, requires much less energy to disperse than the neutral and molecular gas. More recent work shows that jet-induced feedback can indeed impact both warm and cold molecular gas in RGs (Feruglio et al. 2010, 2015; Fischer et al. 2010; Sturm et al. 2011; Dasyra & Combes 2012; Combes et al. 2013; Morganti et al. 2013; Dasyra et al. 2014; Garca-Burillo et al. 2014; Gonzalez-Alfonso et al. 2014; Tadhunter et al. 2014a, 2014b), including turbulence and shock-excited H_2 emission in RGs (e.g., Morganti et al. 2003; Nesvadba et al. 2008, 2011a, 2011b; Guillard et al. 2012, 2015). Molecular hydrogen emission galaxies have large mid-IR H_2 luminosities that are too high for photodissociation regions, and which are most likely generated by jet-generated shocks in the ISM (Appleton et al. 2006; Ogle et al. 2010; Guillard et al. 2012; Lanz et al. 2015). Most of these RGs are in a phase of radio-mode accretion without strong evidence for a concurrent radiative-mode AGN core. Quasar winds may also contribute to molecular outflows in radiative-mode radio AGNs (e.g., Veilleux et al. 2013), such as those we study here; therefore our sample is ideal for studying the relative importance of these two feedback modes in early feedback phases of heavily obscured objects.

1.2. MIR-selected Highly Obscured Quasars

A rare class of highly obscured and luminous quasars at redshifts above 1 was revealed in follow-up studies of extremely red (from the optical to the MIR) sources found in *Spitzer* surveys (Lutz et al. 2005; Yan et al. 2005; Polletta et al. 2006; Dey et al. 2008; Lacy et al. 2011). These systems can have luminosities over $10^{13}\,L_{\odot}$, and deep X-ray observations have revealed Compton-thick AGNs in some ($N_{\mathrm{H}} > 1.5 \times 10^{24}\,\mathrm{cm^{-2}}$; Polletta et al. 2008). The reddest of these *Spitzer*-selected systems are sometimes referred to as dust-obscured galaxies, "DOGs" (Dey et al. 2008).

The *Wide-field Infrared Survey Explorer* (*WISE*), which covers the entire sky at 3.4, 4.6, 12, and 22 μm (henceforth refereed to as the *W*1, *W*2, *W*3, and *W*4 bands) (Wright et al. 2010; Jarrett et al. 2011; Cutri et al. 2012), has opened up the entire MIR sky to searches for obscured QSOs by their MIR signatures (Eisenhardt et al. 2012; Stern et al. 2012, 2014; Wu et al. 2012, 2014; Assef et al. 2013; Bridge et al. 2013; Yan et al. 2013; Jones et al. 2014; Tsai et al. 2015). Although not as deep as the largest *Spitzer* surveys (e.g., Lonsdale et al. 2004; Ashby et al. 2009, 2013), *WISE* is sensitive enough to see the dust thermal emission from the most powerful quasars to redshifts >4. The first results from *WISE* follow-up of the reddest sources (selected without regard to radio brightness) have indeed revealed an extremely IR-luminous population of high-redshift quasars, exceeding $10^{14}L_{\odot}$ in bolometric luminosity in some cases (Eisenhardt et al. 2012; Wu et al. 2012, 2014; Bridge et al. 2013; Jones et al. 2014; Assef et al. 2015; Tsai et al. 2015). Their bolometric luminosities are MIR-

dominated, which led Wu et al. (2012) to dub them "Hot DOGs" (hot dust-obscured galaxies), while Bridge et al. (2013) investigate Lyα Blobs discovered around a high percentage of their red *WISE* sample, the *WISE* Lyman alpha Blobs (WLABs). X-ray observations show only faint fluxes, consistent with highly obscured X-ray AGNs (Stern et al. 2014; Pinconcelli et al. 2015). In this paper we will henceforth refer to the main discovery papers for these *WISE* Hot DOGs and WLABs (Eisenhardt et al. 2012; Wu et al. 2012; Bridge et al. 2013) as EWB12.

1.3. This Work

We present a snapshot survey of 49 sources with the Atacama Large Millimeter/submillimeter Array, ALMA, at 870 μm, which represents a southern sky subset of our sample of 156 radio-powerful (RP) obscured quasar candidates. The sample has been selected to be unresolved in the NVSS and FIRST radio surveys (Becker et al. 1995; Condon et al. 1998) and ultra-red in the *WISE* MIR survey, with similar selection criteria as the Hot DOGs (EWB12), to search for radio-jet dominated feedback from massive, obscured quasars. We also present redshifts obtained from optical and/or near-IR (NIR) spectroscopy for 45 of these ALMA-observed quasars, and additional FIR–submillimeter photometry from other facilities.

The sample is described in Section 2 and the observations in Section 3. The results are presented in Section 4, followed by spectral energy distribution (SED) model fitting and derivation of luminosities and masses in Section 5. The discussion is in Section 6 and conclusions in Section 7. Seven sources with NIR spectroscopy from FIRE on *Magellan* have been discussed by Kim et al. (2013). Jones et al. (2015) have published deep SCUBA 850 μm imaging from the James Clerk Maxwell Telescope (JCMT) for 30 northern sources from our overall sample of 156 RP quasars, detecting four, and finding an excess of serendipitously detected 850 μm sources in the fields on $\sim$1 Mpc scales. Silva et al. (2015) have found an excess of serendipitously detected 870 μm sources in the 49 ALMA images discussed here, in agreement with Jones et al. (2015), although on smaller physical size scales of $\sim$150 kpc, perhaps indicating an excess of starbursting submillimeter galaxies (SMGs) in the fields of these QSOs. Subsequent papers will address Jansky VLA 8–12 GHz imaging of the full sample (Carol J. Lonsdale et al. 2015, in preparation) and VLBA *C*-band imaging of 90 sources, including 33 from the ALMA sample (Colin J. Lonsdale et al. 2015, in preparation). NIR *J* and K_s imaging for a subset of the ALMA sample from Very Large Telescope (VLT)/ISAAC and VLT/XShooter spectroscopy will be presented in A. Blain et al. (2015, in preparation). We adopt a cosmology with $H_0 = 71\,\mathrm{km\,s^{-1}\,Mpc^{-1}}$, $\Omega_\Lambda = 0.73$, and $\Omega_M = 0.27$.

2. SAMPLE SELECTION

For our overall sample of ultra-red, radio-powerful sources, we cross-matched the NVSS catalog, which covers the sky north of $\delta = -40°$, with point sources from the *WISE* Allsky Catalog. The ALMA-observed subsample described here was selected at an earlier time when only the *WISE* Preliminary Catalog was available, as explained further below. Extended *WISE* sources were rejected based on the cataloged `ext` flag. We used positional information from the higher resolution but smaller area FIRST catalog where available, and excluded

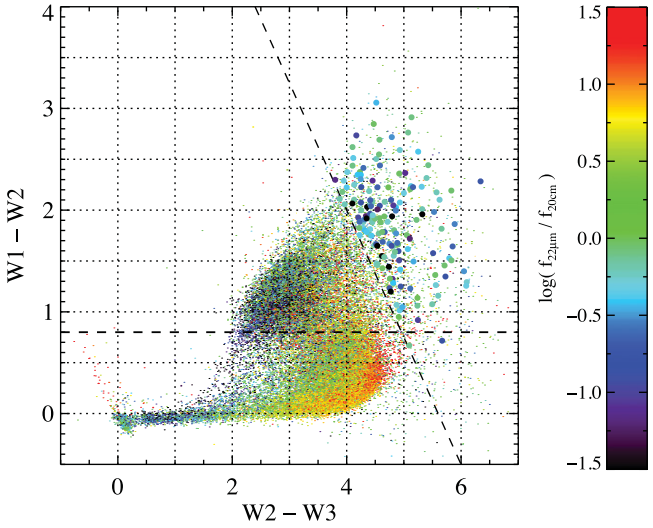

Figure 1. *WISE* 3.4–4.6–12 μm ($W1-W2-$W3) color–color plot (using Vega magnitudes) showing the full *WISE*-NVSS sample of 54,457 sources, color-coded by radio loudness (see Figure 2) as shown by the color bar on the right, radio loudness increasing red to black. The sequence at the bottom is the sequence of normal spirals and starbursts. The flux-limited ultra-red sample of 156 sources is highlighted above the dashed line with larger symbols. The horizontal dashed line shows the AGN color selection criterion used by Stern et al. (2012): $(W1 - W2) > 0.8$, for comparison to our ultra-red selection criterion.

$\pm 10°$ from the Galactic plane. Within this area of 28,443 square degrees of mutual NVSS-*WISE* coverage are 54,457 *WISE* sources that have a robust point source detection (SNR > 7) in the *WISE* 12 μm and/or 22 μm bands and an NVSS/FIRST 1.4 GHz match with a separation of $<7''$, the best compromise between completeness and reliability based on a randomized match analysis. The entire sample is illustrated in the *WISE* 3.4−4.6−12 μm color–color diagram in Figure 1, where we plot the *WISE*-NVSS sample color-coded by $q_{22} = \log(f_{22\ \mu\mathrm{m}}/f_{20\ \mathrm{cm}})$, the 22 μm q parameter, which is a measure of radio loudness (Appleton et al. 2004; Ivison et al. 2007; Ibar et al. 2008). The sequence of low-redshift normal spirals and starbursts has blue $(W1 - W2)$ colors (where *WX* is the Vega magnitude in *WISE* band number X) with a wide range of $(W2 - W3)$ colors, and a cloud of AGNs is seen with redder $(W1 - W2)$ colors (Wright et al. 2010; Jarrett et al. 2011; Yan et al. 2013). The most radio-loud systems are seen toward the left of each of the normal galaxy sequences and the AGN cloud, consisting of the radio-mode and the radiative-mode AGNs, respectively. For low-redshift galaxies the point source fluxes used for this figure may underestimate the total fluxes.

Highly obscured luminous AGNs are expected to be among the reddest sources in this figure. Previous authors have used color cuts in MIR color space and/or MIR–optical space to select the reddest extragalactic *Spitzer* and *WISE* sources (e.g., Dey et al. 2008; EWB12). We have instead chosen to reduce potential bias caused by color cuts, due to the complexity of the observed MIR spectral shape of these sources, which depends strongly on redshift due to the polycyclic aromatic hydrocarbon (PAH) emission features and the 9.7 and 18 μm silicate features. Therefore we have included all sources lying significantly redward of the main *WISE* populations. This is illustrated in Figure 1 by the dashed line, defined empirically as $(W2 - W3) + 1.25\ (W1 - W2) > 7$. The resulting number of sources in the sample redward of our MIR selection threshold

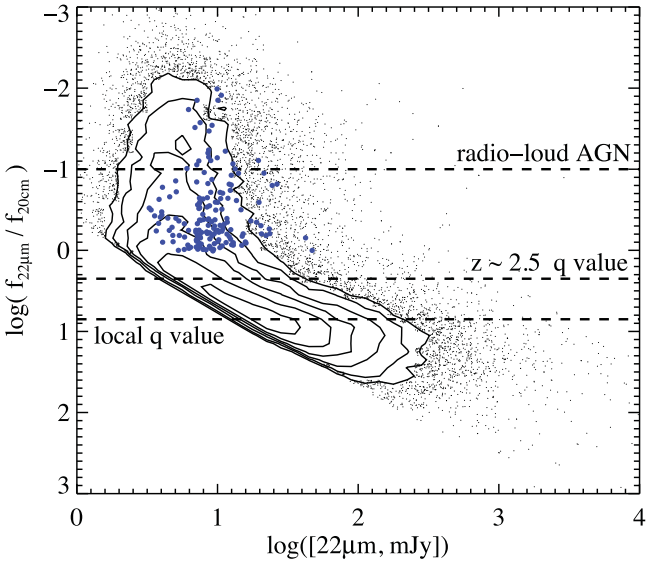

Figure 2. The 22 μm q value, $q_{22} = \log(f_{22\,\mu\mathrm{m}}/f_{20\,\mathrm{cm}})$ vs. *WISE* 22 μm flux density, for the 156 ultra-red, radio-powerful sources (blue points), compared to the full *WISE*/NVSS cross-matched sample of 54,457 sources (dots and contours). The completeness limit of the NVSS is responsible for the diagonal cutoff at the lower left. Also shown are the mean expected values for star-forming galaxies of the infrared-to-radio parameter, $q_{24} = \log(f_{24\,\mu\mathrm{m}}/f_{20\,\mathrm{cm}})$ for the *Spitzer* 24 μm band by Ibar et al. (2008) in the local universe and the k-corrected $z \sim 2.5$ value. The representative radio-loud SED from Elvis et al. (1994) is also shown. The subset of ultra-red sources observed with ALMA was selected to have $0 > \log(f_{22\,\mu\mathrm{m}}/f_{22\,\mathrm{cm}}) > -1$.

in Figure 1 is 1858. To reject radio-quiet systems we added the requirement that $\log(f_{22\,\mu\mathrm{m}}/f_{20\,\mathrm{cm}}) < 0$ as illustrated in Figure 2. For comparison, the color selection criteria for the Hot DOGs of Eisenhardt et al. (2012) and Wu et al. (2012) are either $(W2 - W4) > 8.2$ or $(W2 - W3) > 5.3$, termed by these authors the "W1W2drop" criteria. Bridge et al. (2013) have used a slightly different color selection method: $(W2 - W3) \geqslant 4.8$. Both studies also use brightness or SNR threshold similar to ours, and neither has a radio flux density criterion.

We inspected all candidates in *WISE* and DSS images, and Sloan Digital Sky Survey (SDSS) images where available, rejecting low-redshift galaxies, artifacts, and confused sources. To avoid rejecting galaxies or quasars that could plausibly be within the redshift range of interest, $1 < z < 3$, no specific cut in optical magnitude or MIR/optical flux ratio was imposed. Galaxies with a size or brightness large enough to place them at $z < 0.5$ were rejected, while compact sources with high surface brightness were retained to brighter limits as potential high-redshift quasars. We are obtaining spectra to reject low-redshift sources from our final sample. Thus, our selection can include objects that are less red (in $R - [22]$) than the criterion $(R - [24]) > 14$ used for *Spitzer* DOGs (Dey et al. 2008) and similar samples, and, for example, may include systems in which a massive galaxy dominates the optical light. A total of 708 of the NVSS-*WISE* sample satisfy all our criteria, or ~1.3% of the entire NVSS-*WISE* matched sample. Of the 708 sources, 703 (269) are detected at 12 (22) μm with SNR > 7.

Due to the strongly varying *WISE* sensitivity across the sky, caused by the varying coverage level, a flux density threshold at 22 μm was applied. For the subsample observed with ALMA the flux density threshold chosen was 4 mJy. This was later revised upward to 7 mJy for the remainder of the sample when the Allsky Catalog became available. The final sample is 156 sources, 49 of which belong to the ALMA-observed subsample.

The ALMA subsample fluxes have been revised in the updated *WISE* Allsky Catalog, some now falling below the original 4 mJy threshold. These have been retained in the sample. The decl. range for the ALMA subsample was chosen to allow access to many northern facilities as well as ALMA: $-40° < \delta < +1°$. The ALMA sample is restricted in R.A. to two regions: $3^{\mathrm{h}} <$ R. A. $< 8^{\mathrm{h}}30^{\mathrm{m}}$ and $13^{\mathrm{h}} <$ R. A. $< 21^{\mathrm{h}}$, due to the incompleteness of the *WISE* Preliminary Catalog at that time. Fifty-five sources met our original selection criteria within these areas. Six of these have $\log(f_{22\,\mu\mathrm{m}}/f_{20\,\mathrm{cm}}) < -1$ and were excluded to disfavor classical double-lobed sources, a criterion that was later dropped for the full sample of 156 sources. Of the final ALMA subsample of 49 sources, 48 (23) have SNR > 7 at 12 (22) μm in the *WISE* Allsky Catalog, and the minimum 12/22 μm SNR is 6.7/2.6. Only one source fails the original SNR criterion of SNR > 7 at 12 or 22 μm after the Allsky flux revision: WISE J204049.51–390400.5, which has an SNR at 12/22 μm of 6.7/6.2. Due to the evolving selection criteria the sample is not complete to a fixed SNR or flux density limit.

3. OBSERVATIONS

3.1. FIR and Submillimeter Observations

Twenty-three sources were observed with ALMA in two Band 7 scheduling blocks on 2011 November 16. An additional 14 were observed on 2012 May 25 and the final 12 on 2012 August 29. The central frequency was set to 345 GHz (870 μm), with an 8 GHz bandwidth split into two sidebands. Fifteen antennas were used in the "compact" Early Science configuration for the 2011 November observations, 19 for the 2012 May observations, and 23 for the August observations. The resulting beamsizes are 1.″2, 0.″5, and 1.″2, respectively.

For the November observations, Callisto was used for flux calibration. Titan was used for seven sources in May and Neptune for the other seven sources in May. Titan was again used for all sources in August. The objects were observed with the correlator in time division mode, which results in 256 channels per sideband with a spectral resolution of 14 km s^{-1}. Time on source was 1.5 minute per object, resulting in an rms noise of 0.3–0.6 mJy; the lower noise levels generally correspond to the observations with larger antenna numbers. Flux densities were measured using imfit in CASA, and are reported in Table 1.

Four sources from our overall sample of 156 were observed at 350 μm at the Submillimeter High Angular Resolution Camera II installed at the 10.4 m Caltech Submillimeter Observatory (CSO) telescope (Dowell et al. 2003) on UT 2012 March 22. Two of these, W1343–1136 and W1400–2919, belong to the ALMA subsample. Our observing and data reduction process follows that described by Wu et al. (2012).

Seventy-seven of our full sample of 156 sources, including all the ALMA targets, were queued for *Herschel*[18] PACS (Poglitsch et al. 2010) and SPIRE (Griffin et al. 2010) photometric observations (PID: OT2_clonsdal_1). In total 15 objects were observed by PACS, and five with SPIRE, before

[18] *Herschel* is an ESA space observatory with science instruments provided by European-led Principal Investigator consortia and with important participation from NASA.

Table 1
Optical, *WISE*, NVSS, and ALMA Photometry

WISE Name	*R*-band app. mag. (Vega)	$f_{3.4\ \mu m}$ (mJy) *WISE*	$f_{4.6\ \mu m}$ (mJy) *WISE*	$f_{12\ \mu m}$ (mJy) *WISE*	$f_{22\ \mu m}$ (mJy) *WISE*	q_{22} Observed frame	$f_{1.4\ GHz}$ (mJy) NVSS	$f_{870\ \mu m}$ (mJy) ALMA	log ($f_{870\ \mu m}/f_{22\ \mu m}$)
J030427.53–310838	22.0 ± 0.3	0.179 ± 0.0066	0.693 ± 0.018	4.55 ± 0.12	10.87 ± 0.65	−0.70	54.99 ± 1.72	2.8 ± 0.3	−0.52
J030629.21–335332	20.7 ± 0.2	0.194 ± 0.0070	0.749 ± 0.020	6.19 ± 0.14	4.83 ± 0.65	−0.11	6.17 ± 0.52	1.7 ± 0.4	−0.45
J035448.24–330827	22.5 ± 0.2	0.086 ± 0.0063	0.314 ± 0.015	3.34 ± 0.12	7.05 ± 0.78	−0.04	7.73 ± 0.54	<1.2	<−1.12
J040403.61–243600	20.7 ± 0.2	0.104 ± 0.0072	0.326 ± 0.017	4.63 ± 0.15	4.43 ± 0.92	−0.40	11.04 ± 0.58	3.1 ± 0.4	−0.16
J040937.67–183757	21.3 ± 0.2	0.517 ± 0.0147	2.492 ± 0.054	22.97 ± 0.36	47.07 ± 1.68	0.00	46.91 ± 1.48	<1.5	<−1.47
J041754.10–281654	23.9 ± 0.3	0.043 ± 0.0057	0.143 ± 0.013	1.43 ± 0.10	3.84 ± 0.85	−0.63	16.32 ± 0.68	4.3 ± 0.6	0.05
J043921.92–315908	24.2 ± 0.3	0.034 ± 0.0051	0.090 ± 0.011	1.19 ± 0.09	4.57 ± 0.77	−0.66	20.88 ± 0.78	6 ± 0.4	0.12
J051905.84–081320	>24	0.059 ± 0.0071	0.136 ± 0.015	1.76 ± 0.13	5.09 ± 0.85	−0.72	26.79 ± 0.90	<1.5	<−0.56
J052533.47–361440	22.9 ± 0.3	0.013 ± 0.0053	0.046 ± 0.010	1.38 ± 0.10	4.07 ± 0.71	−0.10	5.12 ± 0.56	<1.5	<−0.41
J052624.72–322500	22.6 ± 0.2	0.023 ± 0.0056	0.106 ± 0.011	6.73 ± 0.17	26.47 ± 1.17	−0.82	173.5 ± 5.23	18 ± 0.5	−0.17
J053622.59–270300	23.2 ± 0.3	0.065 ± 0.0060	0.404 ± 0.016	3.26 ± 0.12	5.35 ± 0.80	−0.18	8.16 ± 0.56	2.7 ± 0.4	−0.30
J054930.07–373939	>24	0.021 ± 0.0049	0.091 ± 0.010	1.09 ± 0.09	3.37 ± 0.73	−0.50	10.60 ± 0.57	2 ± 0.4	−0.23
J061200.23–062209	20.8 ± 0.2	0.330 ± 0.0118	0.621 ± 0.022	9.52 ± 0.20	20.55 ± 1.01	−0.20	32.79 ± 1.08	2.7 ± 0.6	−0.88
J061348.08–340728	>24.6	0.065 ± 0.0065	0.211 ± 0.012	2.62 ± 0.11	7.37 ± 0.71	−0.52	24.15 ± 1.16	<1.8	<−0.62
J061405.57–093658	24.1 ± 0.3	0.017 ± 0.0073	0.069 ± 0.015	2.16 ± 0.14	5.80 ± 0.84	−0.01	5.94 ± 0.51	<1.8	<−0.51
J063027.81–212058	22.2 ± 0.2	0.020 ± 0.0070	0.063 ± 0.014	2.62 ± 0.13	5.06 ± 0.90	−0.39	12.55 ± 0.60	5 ± 1.3	−0.01
J064228.92–272801	21.4 ± 0.2	0.038 ± 0.0070	0.108 ± 0.014	1.33 ± 0.16	3.67 ± 0.87	−0.24	6.36 ± 0.52	2.2 ± 0.6	−0.22
J065215.85–200612	>23.7	<0.013	0.045 ± 0.013	1.92 ± 0.13	4.81 ± 0.83	−0.18	7.35 ± 0.52	3.2 ± 0.5	0.18
J070257.20–280842	21.8 ± 0.2	0.027 ± 0.0061	0.140 ± 0.016	1.76 ± 0.12	4.54 ± 0.86	−0.25	8.00 ± 0.58	<1.8	<−0.40
J071433.54–363552	22.8 ± 0.2	<0.012	0.039 ± 0.011	0.99 ± 0.12	4.01 ± 0.84	−0.47	11.95 ± 0.60	2.4 ± 0.3	−0.22
J071912.58–334944	24.1 ± 0.3	<0.011	0.081 ± 0.012	1.93 ± 0.12	4.06 ± 0.88	−0.78	24.30 ± 0.87	5.2 ± 0.6	0.11
J081131.61–222522	21.5 ± 0.2	0.132 ± 0.0086	0.611 ± 0.023	5.62 ± 0.17	7.61 ± 1.17	−0.37	17.84 ± 0.71	<1.8	<−0.63
J082311.24–062408	22.32 ± 0.16[a]	0.118 ± 0.0078	0.441 ± 0.019	4.08 ± 0.15	10.42 ± 0.97	−0.71	53.99 ± 1.67	<1.8	<−0.76
J130817.00–344754	22.3 ± 0.2	0.086 ± 0.0056	0.248 ± 0.013	3.36 ± 0.12	9.12 ± 0.73	−0.87	68.10 ± 2.10	1.38 ± 0.34	−0.81
J134331.37–113609	21.7 ± 0.2	0.024 ± 0.0057	0.136 ± 0.013	1.61 ± 0.12	3.81 ± 0.79	−0.33	8.18 ± 0.54	2.34 ± 0.31	−0.22
J140050.13–291924	21.7 ± 0.2	0.110 ± 0.0063	0.501 ± 0.018	5.58 ± 0.14	11.85 ± 0.77	−0.64	51.92 ± 1.63	<0.90	<−1.37
J141243.15–202011	…	0.092 ± 0.0063	0.333 ± 0.015	3.39 ± 0.13	7.41 ± 0.78	−0.09	9.01 ± 0.55	2.55 ± 0.63	−0.45
J143419.59–023543	22.02 ± 0.18[a]	0.058 ± 0.0056	0.257 ± 0.014	2.13 ± 0.11	5.04 ± 0.71	−0.86	36.15 ± 1.16	<0.9	<−0.75
J143931.76–372523	…	0.027 ± 0.0071	0.115 ± 0.013	2.34 ± 0.12	3.92 ± 0.83	−0.41	10.02 ± 0.57	<0.6	<−0.75
J150048.73–064939	…	0.068 ± 0.0065	0.293 ± 0.016	6.26 ± 0.17	15.77 ± 0.94	−0.10	20.01 ± 0.73	6.11 ± 0.28	-0.41
J151003.71–220311	…	0.143 ± 0.0095	0.411 ± 0.020	5.34 ± 0.18	14.87 ± 1.09	−0.06	17.14 ± 0.70	<0.9	<−1.27
J151310.42–221004	…	0.037 ± 0.0082	0.214 ± 0.018	2.64 ± 0.16	9.71 ± 1.10	−0.50	30.40 ± 1.03	4.86 ± 0.27	−0.30
J151424.12–341100	…	0.076 ± 0.0091	0.184 ± 0.019	3.12 ± 0.16	7.01 ± 1.03	−0.25	12.39 ± 0.60	<0.9	<−0.94
J152116.59+001755	…	0.039 ± 0.0046	0.274 ± 0.014	5.41 ± 0.15	9.51 ± 0.70	−0.60	37.89 ± 1.20	1.19 ± 0.28	−0.90
J154141.64–114409	…	0.032 ± 0.0077	0.155 ± 0.017	2.91 ± 0.16	10.74 ± 1.14	−0.51	34.52 ± 1.13	1.2 ± 0.3	−1.11
J163426.87–172139	…	0.039 ± 0.0094	0.101 ± 0.018	1.70 ± 0.17	3.57 ± 1.15	−0.42	9.49 ± 0.55	<0.84	<−0.63
J164107.22–054827	…	0.086 ± 0.0083	0.423 ± 0.020	3.14 ± 0.15	6.26 ± 0.89	−0.02	6.62 ± 0.48	2.3 ± 0.29	−0.43
J165305.40–010230	…	0.083 ± 0.0074	0.191 ± 0.015	2.56 ± 0.14	5.31 ± 0.93	−0.36	12.21 ± 0.56	<0.78	<−0.83
J165742.88–174049	…	0.073 ± 0.0102	0.186 ± 0.026	2.82 ± 0.24	8.60 ± 1.01	−0.31	17.48 ± 0.71	<0.78	<−1.04
J170204.65–081108	…	0.021 ± 0.0690	0.074 ± 0.053	3.05 ± 0.26	12.32 ± 1.40	−0.74	67.59 ± 2.07	<1.02	<−1.08
J170325.05–051742	…	0.021 ± 0.0082	0.199 ± 0.018	2.35 ± 0.24	11.66 ± 1.42	−0.39	28.77 ± 0.96	1.02 ± 0.27	-1.05
J170746.08–093916	…	0.119 ± 0.0073	0.342 ± 0.020	3.46 ± 0.28	3.27 ± 1.26	−0.52	10.86 ± 0.52	<1.02	<−0.51
J193622.58–335420	…	0.031 ± 0.0069	0.127 ± 0.016	2.34 ± 0.14	5.27 ± 0.96	0.00	5.27 ± 0.51	1.86 ± 0.36	-0.45
J195141.22–042024	…	0.030 ± 0.0178	0.065 ± 0.036	2.55 ± 0.15	8.56 ± 1.02	−0.38	20.52 ± 1.09	<1.05	<−0.91
J195801.72–074609	…	0.056 ± 0.0086	0.203 ± 0.018	3.29 ± 0.16	7.44 ± 1.06	−0.64	32.79 ± 1.06	<0.93	<−0.90
J200048.58–280251	…	0.027 ± 0.0169	0.113 ± 0.017	3.21 ± 0.17	7.19 ± 1.20	−0.33	15.33 ± 0.66	<0.96	<−0.87

Table 1
(Continued)

WISE Name	*R*-band app. mag. (Vega)	$f_{3.4\ \mu m}$ (mJy) *WISE*	$f_{4.6\ \mu m}$ (mJy) *WISE*	$f_{12\ \mu m}$ (mJy) *WISE*	$f_{22\ \mu m}$ (mJy) *WISE*	q_{22} Observed frame	$f_{1.4\ GHz}$ (mJy) NVSS	$f_{870\ \mu m}$ (mJy) ALMA	log ($f_{870\ \mu m}/f_{22\ \mu m}$)
J202148.06–261159	…	<0.015	<0.065	1.03 ± 0.15	6.27 ± 1.01	−0.04	6.82 ± 0.55	4.4 ± 0.38	−0.15
J204049.51–390400	…	0.070 ± 0.0077	0.254 ± 0.017	2.75 ± 0.15	4.02 ± 0.91	−0.44	10.95 ± 0.57	5.1 ± 0.43	0.10
J205946.93–354134	…	0.052 ± 0.0069	0.182 ± 0.015	2.94 ± 0.14	4.75 ± 0.99	−0.28	9.13 ± 1.07	<0.99	<−0.40

Note.
[a] SDSS *r*-band AB magnitude.

Table 2
Herschel, JCMT, and CSO Photometry

WISE Name	ALMA subsample	Redshift	f_{70} (mJy) PACS	f_{170} (mJy)	f_{250} (mJy) PACS	f_{350} (mJy) SPIRE	f_{500} (mJy) SPIRE/CSO	f_{850} (mJy) SPIRE	JCMT/ALMA
W0524+3005	…	…	92.3 ± 2.1	119.8 ± 7.3	38.9 ± 6.2	<15.9	<19.8	…	
W0526+1259	…	…	31.3 ± 2.0	54.5 ± 7.3	34.3 ± 6.3	18.9 ± 5.2	<19.5	…	
W0537+3947	…	…	33.7 ± 1.7	<26.1	…	…	…	…	
W0541+1130	…	…	23.6 ± 1.8	<30.0	…	…	…	…	
W0844+7420	…	…	106.1 ± 2.0	130.8 ± 6.9	62.0 ± 6.5	44.1 ± 5.4	24.6 ± 6.2	…	
W1001−2141	…	…	…	…	…	<45[a]	…	…	
W1025+6128	…	…	…	…	…	30 ± 13[a]	…	…	
W1331−3913	…	…	<5.7	<24.0	…	…	…	…	
W1332+7907	…	…	56.9 ± 1.5	59.6 ± 7.8	…	…	…	…	
W1343−1136	ALMA	2.49[b]	…	…	…	<45[a]	…	2.34 ± 0.31[c]	
W1400−2919	ALMA	1.67[b]	…	…	…	<45[a]	…	<0.9[c]	
W1500−0649	ALMA	1.500[b]	91.0 ± 3.3	171.6 ± 7.4	…	…	…	6.11 ± 0.28[c]	
W1501+1324	…	0.505[d]	199.9 ± 1.7	200.2 ± 6.9	…	…	…	<6.6[e]	
W1501+3341	…	…	8.1 ± 1.9	49.4 ± 7.0	…	…	…	…	
W1505+0219	…	…	12.2 ± 1.6	50.0 ± 7.9	…	…	…	…	
W1517+3523	…	1.515[d]	53.5 ± 1.6	69.8 ± 8.5	…	…	…	<5.7[e]	
W1921+7349	…	…	19.4 ± 2.0	49.5 ± 7.8	…	…	…	…	
W2005+0215	…	…	14.2 ± 1.9	<21.6	<18.6	<16.2	<19.8	…	
W2059−3541	ALMA	2.380[b]	11.7 ± 2.7	<19.2	<19.2	<16.2	<19.5	<0.99[c]	

Notes.
[a] CSO.
[b] See Table 3.
[c] ALMA 870 μm flux.
[d] Palomar 200 inch.
[e] Jones et al. (2015).

the cryogen depletion of the *Herschel* Telescope in 2013 April. For the PACS observations, two concatenated mini-scans orientated at 70° and 110° were acquired. Each mini-scan has eight legs, a scan length of 3′, and a leg separation of 5″, with a time on source of 220 s. The SPIRE observations were conducted using the small jiggle map mode with two repeats, with 74 s time on source. The data were processed with HIPE 11.1.0. The aperture-corrected flux densities for all 15 *Herschel*-observed sources are presented in Table 2.

Summarizing, the FIR/submillimeter data are available for the 49 ALMA-observed sources discussed in this paper, PACS observations are available for two sources, W1500–0649 and W2059–3541, and SPIRE observations for one, W2059–3541. Two additional sources have upper limits from the CSO at 350 μm, W1343–1136 and W1400–2919.

3.2. Optical and NIR Photometry and Spectroscopy

Redshifts for 45 of the 49 ALMA sources and *R*-band photometry for 26 were obtained and are presented in Tables 1 and 3. In total 48 of the 49 sources were observed spectroscopically, and three of these yielded no line detections. Full details of the spectroscopy will be presented in a later publication; here we make use only of the redshifts. Optical spectra of 23 objects were obtained using the Goodman spectrograph on the SOAR 4.2 m telescope on UT 2012 January 21–24 and UT 2012 December 9–12. The *R*-band photometry obtained with SOAR was taken with the spectrograph acquisition camera. We observed five sources from the *WISE*-NVSS-ALMA sample, and two from the northern JCMT sample, using the Double Spectrograph on the 5 m Hale telescope at Palomar Observatory between 2012 November and 2013 March. As described in more detail by Kim et al. (2013), 24 sources were observed in the NIR with *Magellan* on UT 2012 July 27–29. Finally, 28 sources were observed with VLT/XShooter on UT 2013 June 4–6 and 31 sources were observed in K_s with VLT/ISAAC over three nights from UT 2013 June 1–4, of which 14 were also observed in *J*.

4. OBSERVATIONAL RESULTS

4.1. Photometry and Redshifts

The *R* and *r* magnitudes and the *WISE*, NVSS, and ALMA flux densities for the 49 sources are presented in Table 1. There are 26 ALMA detections at 3σ or above. None of the sources are resolved. The two sources from the ALMA subsample observed with *Herschel* were both detected at 70 μm, and W1500–0649 also at 170 μm (Table 2). Twelve additional sources from the full sample have *Herschel* detections. Neither of the two ALMA sources observed with the CSO, W1343–1136 and W1400–2919, was detected, resulting in 3σ upper limits of 45 mJy for each, while one of the other two souces, W1025+6128, has a modest detection, as listed in Table 2. There are available *R*-band Vega system magnitudes from SOAR for 16 of the ALMA-detected sources and for 10 of the sources with upper limits. W0823–0624 and W1434–0235 have SDSS data in one or more bands. The *R*/*r* magnitudes range from 20.7 to 24.1. The optical photometry is used in this paper only as a rough constraint on the mass of the stellar populations; a full analysis of these data and the NIR photometry will be presented by A. Blain et al. (2015, in preparation).

Redshifts are available for 25 of the 26 detected sources, and for 20 of the 23 sources with ALMA upper limits. Six of the

Table 3
Redshifts, Luminosities and Radio Power

WISE Name	Redshift	log L_{AGN} ($L_\odot$)		log L_{BB} ($L_\odot$)				log L_{Total} ($L_\odot$)			T_{dust} (K)[a]	log $P_{3\ GHz}$ (W Hz^{-1})	q_{22} k-corrected
		Min	Max	30 K	50 K	90 K	120 K	Min	Max	Best	Best model		
W0304–3108	1.54	13.01	13.16	11.49	12.46	12.92	…	13.02	13.36	13.36	90	26.58	−1.30
W0306–3353	0.78	12.19	12.23	10.98	12.07	12.28	…	12.25	12.54	12.53	⟨50,90⟩	24.92	−0.55
W0354–3308	1.37	12.70	12.72	<11.14	<12.14	<12.59	…	<12.71	<12.96	<12.96	90	25.61	−1.15
W0404–2436	1.26	12.58	12.63	11.46	12.48	12.93	…	12.61	13.11	13.11	90	25.67	−1.69
W0409–1837	0.67	12.73	12.74	…	<11.99	<12.4	…	<12.80	<12.90	<12.90	90	25.65	−0.28
W0417–2816	0.94	11.95	12.01	11.48	12.55	12.98	…	12.12	13.02	12.47	⟨30,50⟩	25.54	−1.38
W0439–3159	2.82	13.44	13.45	12.04	12.84	13.33	14.17	13.47	14.24	13.70	90	26.76	−1.12
W0519–0813	2.05[b]	13.01	13.02	<11.30	<12.2	<12.68	<13.58	<13.03	<13.68	<13.18	90	26.53	−1.09
W0525–3614	1.69	12.51	12.60	<11.29	<12.25	<12.71	<13.75	<12.62	<13.77	<12.94	90	25.64	−0.55
W0526–3225	1.98	13.44	13.54	12.40	13.31	13.79	…	13.57	13.95	13.95	90	27.33	−1.18
W0536–2703	1.79	13.05	13.05	…	…	12.94	…	13.00	13.30	13.30	90	25.90	−0.54
W0549–3739	1.71	12.56	12.56	11.39	12.34	12.81	…	12.59	13.00	13.00	90	25.97	−0.92
W0612–0622	0.47	12.03	12.04	10.89	12.05	12.20	…	12.07	12.43	12.43	90	25.14	−0.32
W0613–3407	2.18	13.20	13.20	<11.43	<12.31	<12.79	<13.68	<13.21	<13.80	<13.34	90	26.57	−0.90
W0614–0936	…[c]	12.94	12.95	<11.40	<12.31	<12.78	<13.69	<12.96	<13.76	<13.17	90	25.87	−0.38
W0630–2120	1.44	12.52	12.57	11.72	12.71	13.17	…	12.63	13.26	12.82	⟨30,50⟩	25.86	−1.33
W0642–2728	1.34	12.36	12.36	11.34	12.35	…	…	12.40	12.66	12.66	50	25.50	−1.42
W0652–2006	0.60	11.58	11.59	11.11	12.24	…	…	11.71	12.33	12.12	⟨30,50⟩	24.74	−0.39
W0702–2808	0.94[b]	12.04	12.04	<11.10	<12.17	…	…	<12.09	<12.41	<12.41	50	25.23	−1.00
W0714–3635	0.88	11.88	11.89	11.18	12.26	…	…	11.97	12.41	12.41	50	25.34	−1.09
W0719–3349	1.63	12.57	12.57	…	12.75	13.22	…	12.97	13.31	13.01	⟨50,90⟩	26.71	−1.33
W0811–2225	1.11	12.63	12.63	…	…	<12.65	…	<12.94	<12.94	<12.94	90	25.75	−1.53
W0823–0624	1.75	13.11	13.22	<11.36	<12.3	<12.76	…	<13.12	<13.35	<13.35	90	26.70	−1.10
W1308–3447	1.65	12.99	12.99	11.22	12.18	12.65	…	13.00	13.15	13.15	90	26.74	−1.40
W1343–1136	2.49	13.00	13.02	…	12.43	12.92	13.78	13.12	13.85	13.27	90	26.23	−0.75
W1400–2919	1.67	13.10	13.11	<10.78	<11.73	…	<13.16	<13.11	<13.43	<13.43	120	26.63	−1.13
W1412–2020	1.82	13.02	13.17	11.52	12.45	12.92	…	13.03	13.36	13.36	90	25.95	−0.43
W1434–0235	1.92	12.89	12.89	<11.08	<12.00	<12.47	<13.39	<12.90	<13.51	<13.03	90	26.62	−1.22
W1439–3725	1.19	12.29	12.29	<10.79	<11.81	<12.26	…	<12.30	<12.58	<12.58	90	25.58	−1.70
W1500–0649	1.50	13.07	13.50	…	12.84	13.33	…	13.52	13.59	13.52	90	26.10	−0.89
W1510–2203	0.95	12.60	12.61	<10.74	<11.81	<12.23	…	<12.62	<12.76	<12.76	90	25.57	−0.84
W1513–2210	2.20	13.26	13.26	11.86	12.74	13.22	…	13.28	13.54	13.54	90	26.68	−0.89
W1514–3411	1.09	12.44	12.48	<10.81	<11.86	<12.29	…	<12.45	<12.70	<12.70	90	25.57	−1.36
W1521+0017	2.63[b]	13.61	13.61	…	…	12.63	…	13.65	13.65	13.65	90	25.60	−1.04
W1541–1144	1.58	12.81	12.94	11.13	12.10	12.57	…	12.95	13.01	13.01	90	26.40	−1.15
W1634–1721	2.08	12.83	12.83	<11.08	<11.98	<12.46	<13.36	<12.84	<13.47	<12.98	90	26.11	−0.80
W1641–0548	1.84	12.94	13.09	…	12.41	12.88	…	13.05	13.30	13.30	90	25.83	−0.37
W1653–0102	2.02	13.00	13.00	<11.04	<11.94	<12.41	<13.31	<13.00	<13.48	<13.10	90	26.19	−0.73
W1657–1740	…[c]	13.16	13.17	<11.03	<11.94	<12.42	<13.32	<13.17	<13.55	<13.60	⟨90,120⟩	26.34	−0.68
W1702–0811	2.85	13.60	13.60	<11.28	<12.07	-…	<13.4	<13.60	<13.81	<13.81	120	27.26	−1.20
W1703–0517	1.80[b]	13.11	13.51	11.12	12.05	12.48	13.45	13.12	13.61	3.60	⟨90,120⟩	26.91	−0.74
W1707–0939	…[c]	12.98	13.04	<11.15	<12.06	<12.54	<13.43	<12.99	<13.56	<13.56	120	26.14	−0.89
W1936–3354	2.24[b]	13.05	13.18	11.45	12.32	…	13.69	13.06	13.78	13.78	120	25.64	−0.40
W1951–0420	1.58	12.80	12.83	<11.08	<12.05	…	<13.45	<12.84	<13.54	<13.54	120	26.18	−1.03
W1958–0746	1.80	12.98	12.98	<11.08	<12.01	<12.48	<13.41	<12.99	<13.54	<13.10	90	26.51	−0.99
W2000–2802	2.28	12.75	12.90	<10.72	<11.59	<12.07	<12.96	<12.75	<13.17	<12.96	90	25.99	−0.73

Table 3
(Continued)

WISE Name	Redshift	log L_{AGN} ($L_\odot$)		log L_{BB} ($L_\odot$)				log L_{Total} ($L_\odot$)			T_{dust} (K)[a]	log $P_{3\ GHz}$ (W Hz^{-1})	q_{22} k-corrected
		Min	Max	30 K	50 K	90 K	120 K	Min	Max	Best	Best model		
W2021–2611	2.44	12.97	13.51	11.85	12.68	…	14.04	13.00	14.15	14.15	120	25.93	−0.45
W2040–3904	…[c]	12.92	13.15	11.85	12.76	13.23	…	12.96	13.49	13.49	90	26.14	−0.81
W2059–3541	2.38	13.15	13.37	…	…	<12.46	<12.87	<13.15	<13.42	<13.42	90	26.26	−0.69

Notes.
[a] ⟨T1,T2⟩ denotes an average between these two model fits.
[b] Uncertain redshift: single line, blended lines, or weak lines.
[c] $z = 2$ assumed if no spectroscopic redshift exists.

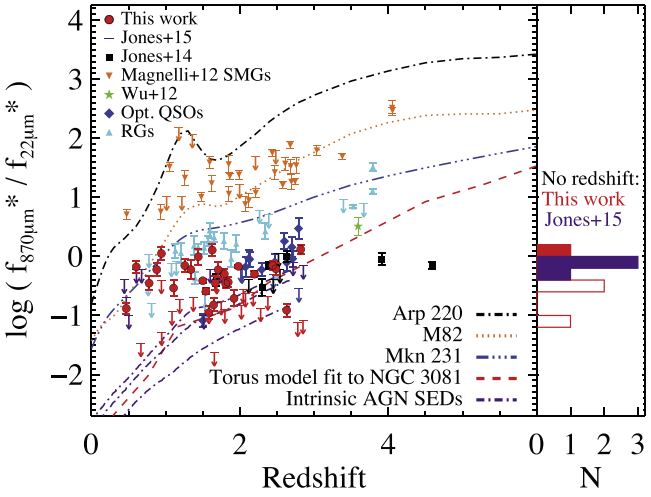

Figure 3. Ratio of ALMA 870 μm to *WISE* 22 μm flux density vs. redshift for the ALMA sample (red points and limits). Histogram: sources without redshift (submillimeter-detected sources: filled bars; upper limits: empty bars). The comparison templates and source samples are described in the text. The three intrinsic AGN curves (purple dashed–dotted lnes) are the mean[log($L_{2-10\ \mathrm{kev}}$/erg s^{-1}) < 42.9], mean[all], mean[log($L_{2-10\ \mathrm{kev}}$/erg s^{-1}) > 42.9] SEDs of Mullaney et al. (2011) in descending order which cover the 6–1000 μm rest frame; the full dispersion of intrinsic AGN SEDs reported in that paper is significantly wider. The three ALMA sources lying on or above the Mkn 231 template are W0417–2816, W0652–2006, and W0714–3635. *: The comparison samples include data at 850 μm and at 24 μm.

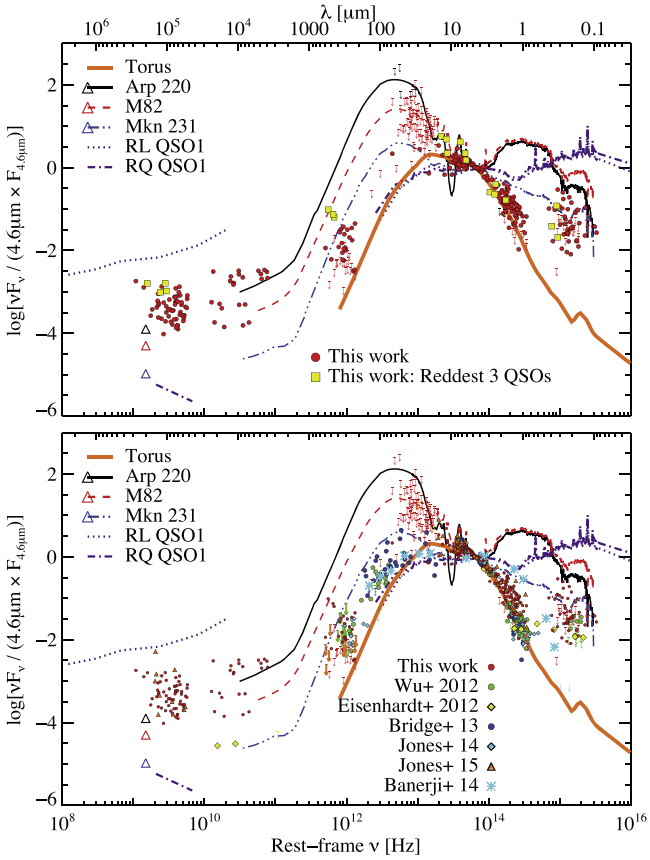

Figure 4. Rest-frame ensemble SEDs for *WISE*-selected ultra-red systems. Top: the 45 sources in our ALMA sample with known redshift, normalized at 4.6 μm, compared with the templates from the library of Polletta et al. (2007), the torus model fitted to one of our sources in Section 5.2.1, and the intrinsic AGN SEDs of Shang et al. (2011) (labelled RQ QSO1 and RL QSO1). The colored triangles in the radio correspond to the matched color template. The three reddest objects, relative to Mkn 231, from Figure 3 are highlighted in yellow. The upper limits in the rest ∼12–100 μm range are largely from *IRAS*, with a few from *Herschel* (see text for details). Several sources lie at redshifts where the 22 μm band coincides with the 9.7 μm silicate absorption feature, which may partially account for the turnover in their spectral shapes. Note the intermediate radio power compared to classical (evolved) RQ and RL QSOs, when normalized to 4.6 μm power. Bottom: Rest-frame SEDs for the *WISE*-selected red Hot DOG sources from Wu et al. (2012) (green circles), Eisenhardt et al. (2012) (yellow diamonds), Jones et al. (2014) (cyan diamonds), and the WLABs from Bridge et al. (2013) (blue circles) compared to our samples (red circles, orange triangles; Jones et al. 2015). Also shown are the reddest of the dust-reddened type 1 quasars from Banerji et al. (2014) (cyan asterisks).

nineteen sources in Table 2 have known redshifts, including the four sources in the ALMA subsample and the two JCMT-observed sources. It is beyond the scope of the present paper to analyze the optical/NIR spectroscopy, but we note that many spectra have indications from the ionization levels of an obscured radiative-mode AGN (Baldwin et al. 1981; Kewley et al. 2013). The *Magellan*/FIRE observations have been published by Kim et al. (2013) while the VLT/Xshooter observations will be reported by A. Blain et al. (2015, in preparation). One object was not observed (W1657–0102), one was not detected even in continuum (W0614–0936), and for two objects only a faint continuum was detected (W1707–0811 and W2040–3541). Additionally the redshifts are uncertain for five sources that have only weak lines, a single line detection, or an unresolved line pair. They are: W0519–0813 (Lα λ1216 Å), W0702–2808 ([O II]λ3727 Å), W1521+0017 (weak Hβ, [O III] λ4959, 5007 Å), W1703–0517 (blended Hα + [N II] λ6584 Å), and W1936–3354 ([O II] λ3727 Å).

4.2. Colors and SEDs

The ALMA observations were designed to constrain the luminosity of these quasars in the rest-frame FIR–submillimeter compared to the MIR. We will show that most of our *WISE*-NVSS-ALMA sample have SEDs dominated by an AGN in the MIR, and possibly through the FIR–submillimeter also. However, substantial rates of star formation are likely also present.

We present the main results in Figures 3–5. We show these results in two complementary ways: (1) the ratio of 870 μm/22 μm flux density as a function of redshift is shown in Figure 3, and (2) we use the range in redshifts for the sample to construct an "ensemble" rest-frame SED for our sample in Figure 4. We show ensemble SEDs of several comparison samples in Figure 5. In all the plots we also show the tracks for several templates of nearby well studied sources. The ensemble SEDs must be interpreted carefully because the choice of normalization wavelength affects the relative appearance of dispersion between the points at other wavelengths. We have chosen to normalize the templates and data at rest-frame 4.6 μm. The selection of 4.6 μm has the disadvantage that this spectral region may suffer significant extinction from a thick torus or other nuclear dusty structure, but it is the longest wavelength (and hence has the lowest optical depth) that avoids the PAH and silicate features yet still lies within the *WISE* rest-frame wavelength range for all of the ALMA sources.

The source templates in all five figures are from Polletta et al. (2007), and include the cool starburst-dominated ultra-luminous infrared galaxies (ULIRG) Arp 220, the starburst M82, and the broad-line dusty QSO Mrk 231. The torus model in Figures 4 and 5 is based on the tapered disk models of

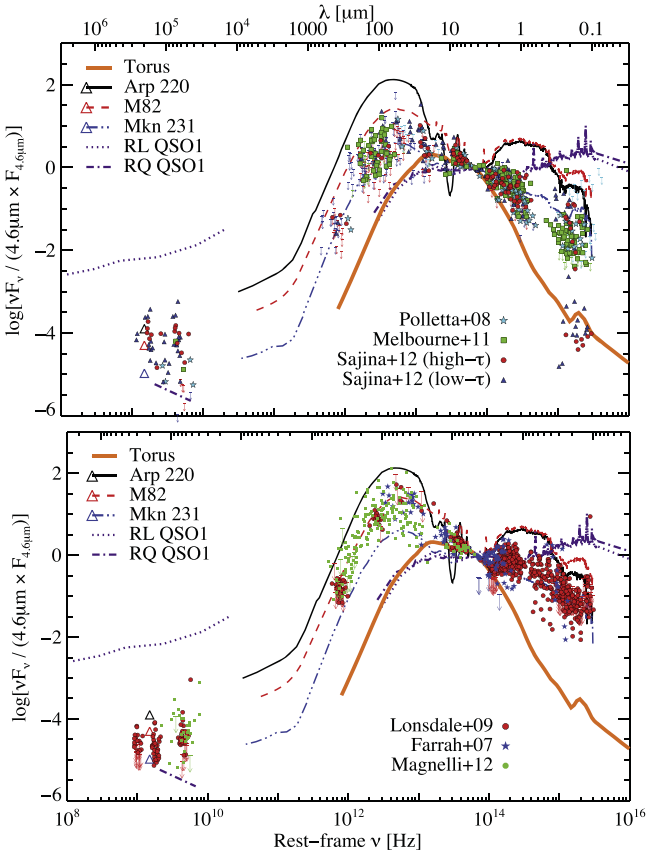

Figure 5. Rest-frame SEDs for several comparison *Spitzer* and *Herschel* samples. Top: rest-frame SEDs for 152 *Spitzer* DOGs which were selected in a similar manner to our sample (Polletta et al. 2008; Melbourne et al. 2012; Sajina et al. 2012). The extreme redness in the UV–optical for many of the Sajina et al. (2012) sources is due to their selection criteria. Bottom: rest-frame SEDs for 61 high-redshift MIR-selected starburst-dominated ULIRGs from Lonsdale et al. (2009) and Fiolet et al. (2009) (red symbols), 16 *Spitzer* 70 μm selected galaxies from Farrah et al. (2007) (blue symbols) and 61 SMGs with *Herschel* data from Magnelli et al. (2012) (green symbols).

Efstathiou & Rowan-Robinson (1995) and has been fitted to one of our best sampled SEDs in this paper (see Section 5.2.1). This torus model has an opening angle of 45°, an inclination angle of 54° and a UV equatorial optical depth $\tau_\nu = 500$. The intrinsic AGN SEDs, from Shang et al. (2011) and Mullaney et al. (2011), are empirical SEDs of nearby AGNs from which the host galaxy light has been subtracted, and they are quite similar to each other and to other published intrinsic AGN SEDs (Elvis et al. 1994; Richards et al. 2006; Netzer et al. 2007; Assef et al. 2010). In Figure 3 we include the modeled SED of a dust torus of ∼4 pc radius in the nearby AGN NGC 3081 that Ramos-Almeida et al. (2013) derived based on *Herschel* data and subarcsecond MIR imaging with Gemini T-ReCS.

Most of our *WISE*-NVSS-ALMA sample is much more strongly MIR-dominated than the starburst templates (M82 and Arp 220) in Figure 3, and also compared to the $1 < z < 3$ SMGs (Magnelli et al. 2012), which we illustrate to provide a comparison to high-redshift starburst-dominated systems. The *WISE* radio-blind Hot DOG samples (EWB12; Jones et al. 2014) and our northern sample of RP sources (Jones et al. 2015) are similar to the ALMA sample in showing a low submillimeter/MIR flux density ratio compared to the galaxy templates. Generally speaking, the *WISE* sources lie between the intrinsic SEDs and the Mkn 231 template, though some of the upper limits lie below even the intrinsic SEDs shown. We also show some representative redshift ∼1–3 RGs (Archibald et al. 2001; Grimes et al. 2005; Seymour et al. 2007) and broad-line (optically selected) quasars (Priddey et al. 2003, 2007) with available 850 μm data in the plot, but a detailed comparison to the FIR–submillimeter properties of well selected samples of AGNs of various types is beyond the scope of this paper. The broad-line QSOs shown tend to have similar colors to our sample, while the RGs shown tend to be a bit more FIR-strong relative to the MIR, but these trends may be dominated by selection effects and should be used only as a very general comparison to our sample.

The conclusions from Figure 3 are emphasized in the ensemble SED (Figure 4-*top*), where we see a strong similarity among the MIR–submillimeter SEDs of the ALMA sample. They resemble the torus model with high optical depth in the rest-frame NIR–MIR, as expected since this model was designed to fit one of our sources, but they are systematically *steeper* than any of the galaxy or intrinsic AGN templates in this wavelength range, when normalized at 4.6 μm. There is a lack of observational data available in the rest-frame FIR, although the *IRAS* limits (red limits at $10 < \lambda_{\rm rest} < 100$ μm) help to constrain the flux of many of our *WISE*-NVSS sample, ruling out SEDs like Arp 220 and M82.

The three sources with highest submillimeter/MIR flux ratios (relative to the templates) from Figure 3, W0417–2816, W0652–2006, and W0714–3635 (yellow points in Figure 4), are the strongest candidates for possessing significant ongoing star formation. Their presence in our sample may be the result of a selection effect due to strong 6.7–7.7 μm PAH features falling in the *W*3 filter, or an 11.7 μm PAH feature falling in the *W*4 filter, as can be seen in Figure 4.

In Figure 4-*bottom* we add the ten sources with known redshift from Jones et al. (2015) (orange triangles), which are drawn from our northern *WISE*-NVSS sample. They all have upper limits at 850 μm from JCMT and they show very similar SEDs to the ALMA subsample. We also compare our radio-selected samples to the radio-blind *WISE* Hot DOG samples of EWB12 and of Jones et al. (2014). We see a very close similarity between the radio-selected (red and orange symbols) and radio-blind samples (green, blue, cyan, and yellow filled symbols). The radio-blind Hot DOG samples have systematically larger redshifts than our sample, displacing the two sets of SEDs from each other in rest wavelength somewhat, but the radio-selected and radio-blind samples fall within a continuous band. The different redshift selection function for the two samples may be unrelated to radio power, instead being due at least in part to the redder ($W2 - W3$) threshold of EWB12. This probably eliminates sources with silicate absorption that falls into the 22 μm filter, and therefore favors sources with $z \gtrsim$ 1.5–2. Jones et al. (2015) have suggested that the northern sources from our NVSS-*WISE* sample that they observed at 850 μm at the JCMT may show slightly less steep rest-frame SEDs than the EWB12 samples. This is an interesting possibility that requires further study.

The *WISE* samples of EWB12 have more data from *Herschel* in the rest MIR–FIR than we do for our sample, and their ensemble FIR SEDs tend to fall in the region occupied by the intrinsic SEDs, the torus template, and the Mkn 231 template (Figure 4). The two *WISE*-NVSS sources for which we have *Herschel* data fall in the same region. All of these sources lie

well below both M82 and Arp 220 in this wavelength region, emphasizing the result from Figure 3. The limited *Herschel* data that we do have for our sample, and the *IRAS* limits, support a picture in which our *WISE*-NVSS sample has similar FIR–submillimeter SEDs to the radio-blind *WISE* samples. The one Hot DOG with published radio data (Eisenhardt et al. 2012) has lower radio power than our sample, when normalized to 4.6 μm power.

It is interesting to compare the *WISE*-NVSS objects to the reddest known broad-line type 1 quasar from Banerji et al. (2014), ULAS J1234+0907 ($z = 2.50$), shown as the cyan asterisks in Figure 4-*bottom*. The SED shape is very similar to the Hot DOGs through the MIR–submillimeter but is much less red than any of the *WISE* sample in the rest NIR 1–5 μm region. Unlike the *WISE* red sample, ULAS J1234+0907 follows the Mkn 231 template through $\sim$1 μm, only dropping steeply at shorter wavelengths. The best fit model by Banerji et al. (2014) has $A_V = 6$. This result emphasizes the likelihood that the steep red *WISE*-optical SEDs for the *WISE*-selected samples are caused by heavy obscuration.

In Figure 5-*top* we turn to a comparison to the *Spitzer*-selected "power-law" DOGs (Polletta et al. 2008; Melbourne et al. 2012; Sajina et al. 2012), including the two $z > 3$ Compton-thick quasars discussed by Polletta et al. (2008). As a class the *WISE* samples show significantly redder ensemble rest NIR slopes than most of the *Spitzer* DOG samples. The *WISE* sources also appear to turn over into the FIR/submillimeter at systematically shorter wavelength than the DOGs, as can be seen by comparing Figures 4-*bottom* and 5-*top*, and as previously discussed by EWB12 and Jones et al. (2014, 2015). To first order, this is likely to indicate a larger ratio of star formation to AGN accretion in the *Spitzer* DOGs than in the Hot DOGs.

Lastly we illustrate in Figure 5-*bottom* the ensemble SEDs of several samples of *Spitzer*-selected starburst-dominated ULIRGs (Farrah et al. 2007; Fiolet et al. 2009; Lonsdale et al. 2009) and SMGs observed with *Herschel* (Magnelli et al. 2012). These samples have more marked FIR emission than either the *WISE* sources or the *Spitzer*-selected DOGs, relative to MIR emission, and bluer optical–MIR SEDs.

Turning to the centimeter–radio emission, there is a steady decrease in the average radio/4.6 μm flux density ratio from our sample through the *Spitzer* DOGs to the SMGs/starbursts, although there is a lot of overlap between the latter two samples. This in entirely consistent with the selection in favor of bright radio sources in our sample, and the dominance of star formation in the SMGs and starbursts.

In summary, the *WISE*-selected ultra-red samples have very similar SED shapes from the rest-frame NIR through the FIR, with no obvious difference between the radio-selected samples (this paper and Jones et al. 2015) and the radio-blind Hot DOGs (EWB12; Jones et al. 2014) except that the radio-blind samples have a larger mean redshift, which may be caused by the different selection functions. Together, these sources are redder than any other known source type in the NIR–MIR, and most of them turn over into the FIR at higher frequencies than the Spitzer DOGs, starbursts, and SMGs.

4.3. Synchrotron Contribution to the ALMA fluxes

Before addressing the possible range of SFRs in these sources, we first consider the possibility that a fraction of the 345 GHz flux is due to synchrotron emission. Since we have selected compact radio sources in radiatively efficient AGNs there is the possibility that the radio emission is beamed and that some of our sources are blazars. We briefly address the possibility that some of the 345 GHz emission arises from non-thermal synchrotron emission associated with the radio sources here, but we defer detailed discussion of this topic to the next paper in our series, in which we present the high-resolution *X*-band (8–12 GHz) imaging from the VLA.

We can draw some preliminary conclusions from the measured spectral indices across the 8–12 GHz VLA *X*-band, which are more reliable than indices derived from non-contemporaneous and non-beam-matched 1.4 GHz NVSS data and the much later *X*-band imaging. We find that the majority of the sample has steep spectral indices between 8 and 12 GHz; 42 of them have $\alpha_{12}^{8} < -0.8$ (27 have indices steeper than -1.0), characteristic of optically thin synchrotron emission and potentially consistent with being Gigahertz Peaked Sources (<1 kpc in size with a synchrotron peak $\sim$1 GHz) or Compact Steep Spectrum sources (CSS; <20 kpc in size with a synchrotron peak below 1 GHz) (O'Dea 1998). Several sources are also resolved or multiple on scales of 1–10 kpc. For most of these steep spectrum sources the synchrotron contribution to the 345 GHz flux is likely to be <10%.

The remaining seven sources have flat or inverted 8–12 GHz spectral indices, but two of these show a steepening spectral index between 12 and 20 GHz (from our limited VLA *K*-band imaging), thus they are also likely to be dominated by optically thin synchrotron emission (W0526–3225 and W0823–0642). Two of the remaining five sources (W0642–2728 and W1434–0235) have an ALMA measurement (a detection and a limit, respectively) that is well in excess (by a factor of five or more) of the extrapolated flat radio SED. The other three sources (W0536–2703, W1412–2020, and W1634–1721) require a synchrotron peak beyond 12 GHz to avoid exceeding the ALMA flux density detection or limit, and these are also probably not blazars unless they are exceptionally variable. They are more likely to be High Frequency Peakers (small <100 pc sources with synchrotron peaks above 4 GHz; Dallacasa et al. 2000) and it is possible that their 345 GHz flux has a significant contribution from optically thin synchrotron emission. None of the flat or inverted spectrum sources has a plausible SED that can explain the *WISE* data as synchrotron emission from a blazar.

5. ISM MASS, SED FITS, AND DERIVED PARAMETERS

As noted in the previous section, the simplest description of the NIR–FIR SED shapes of the majority of our sample is that they resemble the intrinsic shapes of local AGN samples, derived by subtracting the host galaxy emission (Elvis et al. 1994; Richards et al. 2006; Netzer et al. 2007; Assef et al. 2010; Mullaney et al. 2011; Shang et al. 2011). If we interpret the SEDs in this fashion then we could conclude that *all* of the MIR–submillimeter dust emission stems from re-radiation of accretion disk energy by a nuclear torus or other dusty structure. In this section we explore, as an alternative, the range of plausible contributions from star formation that may be permitted by reasonable models of the SEDs.

5.1. Interstellar Medium Mass

We derive the ISM masses assuming that 100% of the 345 GHz flux is thermal dust emission. As noted in the

previous section the thermal fluxes could be overestimated by <10% for most of the sample due to possible contributions from synchrotron emission, and by up to 100% for three sources. We do not correct the data for this contamination because it is highly uncertain at this point in time.

Scoville et al. (2014) derive the gaseous ISM mass ($M_{\rm HI} + M_{\rm H_2}$) of populations of distant galaxies in the COSMOS field using ALMA 870 μm data as a measure of cool dust mass. They use a local sample of well studied galaxies to show that the observed ratio of 850 μm specific luminosity to ISM mass is $L_{\nu 850\,\mu{\rm m}}/M_{\rm ISM} = 1 \pm 0.23 \times 10^{20}$ erg s^{-1} Hz^{-1} $M_\odot^{-1}$ for low-redshift spirals, with a dispersion of a factor of about 5. Using this empirical calibration, Scoville et al. (2014) derive the following relation for a flux density measured at observed frequency $\nu_{\rm obs}$ (valid for $\lambda_{\rm rest} > 250$ μm on the Rayleigh–Jeans tail where the emission will be optically thin) to derive ISM masses from ALMA data for SMGs (their Equation (12), valid for a dust temperature of 25 K):

$$\frac{f_{\nu_{\rm obs}}}{\rm mJy} = 0.83\,\frac{M_{\rm ISM}}{10^{10}M_\odot}\,(1+z)^{4.8}\left(\frac{\nu_{\rm obs}}{\nu_{850\,\mu{\rm m}}}\right)^{3.8}\frac{\Gamma_{\rm RJ}}{\Gamma_0}\left(\frac{\rm Gpc}{d_{\rm L}}\right)^2. \quad (1)$$

Here $\Gamma_{\rm RJ}/\Gamma_0$ corrects for the departure of the dust emission spectrum from the Rayleigh–Jeans tail as the redshift increases from 0 (and the rest frequency approaches the peak of the spectrum) and $d_{\rm L}$ is the luminosity distance. Scoville et al. (2014) adopt 250 μm as the minimum acceptable rest-frame wavelength for derivations of ISM mass, thus we expect our results to provide reasonable estimates for sources with $z < 2.5$, which represents 94% of our sample, with only small inaccuracies for the three sources with $2.5 < z < 2.85$. $\Gamma_{\rm RJ}$ is a function of assumed dust temperature, which was taken to be 25 K by Scoville et al. (2014). The constant 0.83 in the equation is also proportional to $T_{\rm d}$. We derive ISM masses (Table 5, columns 13 and 14), for dust temperatures of 30 and 90 K, using the appropriate values for the constant, Γ_0, and $\Gamma_{\rm RJ}$. The majority of the dust in these systems is unlikely to be as warm as 90 K, therefore these values provide fairly strong lower limits to the ISM masses when we have an 870 μm detection. We estimate the overall uncertainty to be a factor of five, based on the unknown dust temperature and the overall dispersion for local starburst systems in Figure 1 of Scoville et al. (2014).

The ISM masses for $T_{\rm d} = 30$ K range from 0.8 to 56 $\times 10^{10}$ $M_\odot$, with a median for the 26 ALMA-detected sources of 5.9×10^{10} $M_\odot$. This may be compared to the values derived by Scoville et al. (2014) for their mid- plus high-redshft sample galaxy stacks from the COSMOS field, which cover a similar redshift range to our sources. Their "IR Bright" sample has a median ISM mass of $(11.91 \pm 0.77) \times 10^{10}$ $M_\odot$, about twice that of our sample.

5.2. SED Fits

The SEDs of most of the red *WISE*-NVSS sources are dominated by warm dust in the MIR with a strong decline into the submillimeter, and many of them display spectroscopic evidence of an obscured, high excitation AGN. The minimum AGN luminosity can be reasonably well determined from the warm dust emission that dominates the *WISE* data. The total 1–000 μm luminosity is less well constrained, however, for most sources, because we lack data in the rest-frame FIR. We can model the emission by assuming a dominant dust temperature, $T_{\rm d}$, for the cooler dust that peaks in the FIR wavelength range, but the luminosity of such a component depends on the fourth power of $T_{\rm d}$, and is uncertain by 2–3 dex without measurements at the FIR peak of the dust SED.

Two sources have available *Herschel* data, W1500–0649 and W2059–3541, and for these we find that the SED shapes fall well below the SEDs of M82 and Arp 220 longward of the MIR, resembling the radio-blind-selected Hot DOGs (Figure 4). We have constructed radiative transfer (RT) models for W1500–0649 ($z = 1.50$), which has the most detections (seven bands in total) that include good constraints on the peak of the SED, in order to provide some insights into the nature of these sources. For the remaining sample there are insufficient data points to justify RT models, therefore we use a parametric "torus" model plus modified blackbody (BB) fits for the cooler dust.

5.2.1. RT Model for WISE 1500–0649

We have constructed example models for W1500–0649 using both a tapered disk model (Efstathiou & Rowan-Robinson 1995) for the torus (see also Efstathiou et al. 2013) and the two-phase clumpy torus models of Stalevski et al. (2012). For the cooler dust component radiating in the FIR we use the starburst models of Efstathiou et al. (2000) which were revised by Efstathiou & Siebenmorgen (2009).

The tapered disk models have four parameters plus a normalization factor and the starburst models have three parameters plus a different normalization factor. In the tapered disc AGN models we fix the opening angle of the torus Θ_0 at 45° and vary the equatorial optical depth of the torus $\tau_{\rm uv}^{\rm eq}$ in the range 250–1250 ($A_V \approx$ 50–250), the inclination i in the range 45°–90°, and the ratio of outer torus radius to inner radius r_2/r_1 from 20 to 160. In the starburst models we fix the initial optical depth of the molecular clouds τ_V at 75 (which is the average value in the model grid) and the e-folding time of the starburst at 20 Myr, which from previous work appears to be a reasonable timescale for starbursts (e.g., Efstathiou et al. 2000). In the starburst models we only vary the age of the starburst t_*.

We use a standard χ^2 minimization technique to find the model parameters that best fit the data. The best tapered disk fit is shown in Figure 6-*top* (the AGN torus model is plotted with a blue dotted line and the starburst model with a red dashed line) and assumes the following parameters: $\tau_{\rm uv}^{\rm eq} = 500$, $r_2/r_1 = 160$, $i = 54°$, and $t^* = 15$ Myr.

The AGN torus has a derived luminosity of 1.9×10^{13} $L_\odot$. This needs to be multiplied by the anisotropy correction factor A (Efstathiou 2006), which for this particular combination of parameters is 0.84, to give an AGN luminosity of $1.6 \times 10^{13} L_\odot$. The starburst luminosity is 1.8×10^{13} $L_\odot$ so the total luminosity of the system is predicted to be 3.4×10^{13} $L_\odot$.

In Figure 6-*bottom* we show the SED of W1500–0649 fitted with the two-phase clumpy torus models of Stalevski et al. (2012) in combination with the starburst models of Efstathiou & Siebenmorgen (2009). We find that a good fit can be obtained with a torus that assumes a half-opening angle of 50° and an inclination of 90°. The AGN luminosity is predicted to be 1.2×10^{13} $L_\odot$ and the starburst luminosity 2.4×10^{13} $L_\odot$. The starburst is still predicted to be a young system with an age of 10 Myr. We conclude that, irrespective of the uncertain dust

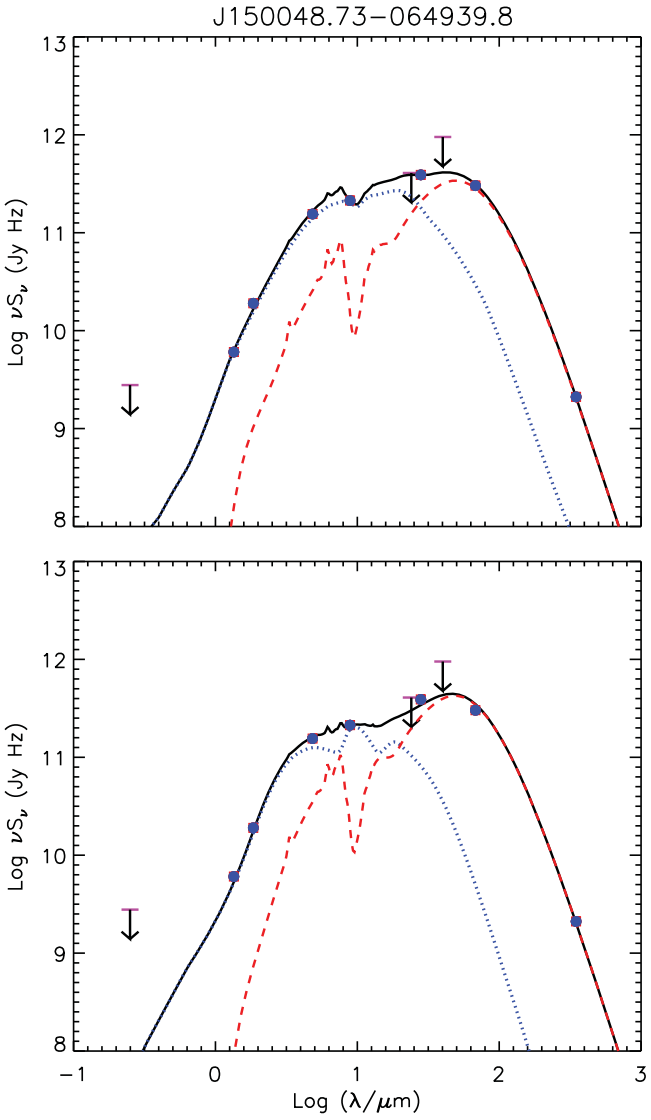

Figure 6. Best-fit radiative transfer models for WISEJ150048.73–064939.8. Top: AGN tapered disk model of Efstathiou & Rowan-Robinson (1995) which has $\tau_{uv}^{eq} = 500$, $r_2/r_1 = 160$, $i = 54°$, and $t_* = 15$ Myr. Bottom: AGN clumpy torus model of Stalevski et al. (2012) (blue dotted lines). The starburst models (red dashed lines) are from Efstathiou & Siebenmorgen (2009).

geometry, in W1500–0649 the AGN and the starburst emit comparable luminosity.

5.2.2. Three-component SED Fits

We model the full sample by fitting the minimum number of simple spectral components to the SEDs that will define a reasonable *maximum* SFR that is consistent with the observed data, and to provide minimum and maximum estimates of the luminosity of the AGN-heated dust. A third SED component in the optical is used to estimate stellar mass, and we assume the AGN is completely obscured in the optical–UV. The results are presented in Tables 3–6 and illustrated in Figure 8. A more thorough analysis of the SEDs using RT models for the full sample is in preparation by A. Efstathiou et al.

The method fits a parameterized "torus" model to the MIR data and a modified blackbody (BB) to the longer wavelength SED. The "torus" model could describe a classical torus, or some other dusty structure heated by the AGN, including a spherical "cocoon" with 100% covering factor of warm dust, Ω_{WD}. For the BB component the characteristic dust temperature is undefined for most sources, therefore we construct four models with different fixed dust temperatures. Modeling a range of dust temperatures within an individual source is not justified by the available data points. We do not expect all sources to be fitted well for each of these temperature choices, particularly the higher values, and we carry forward into the analysis only those SED fits that are viable.

The methodology follows Sajina et al. (2012) but is simplified from their four dust components to only two, due to the limited SED data available for our sample. The AGN MIR emission is modeled with a parameterization that is consistent with the clumpy torus models of Nenkova et al. (2008). It has the functional form

$$f_\nu = \frac{\nu}{\left(\frac{\nu}{\nu_0}\right)^{\alpha} e^{0.5\nu} + \left(\frac{\nu}{\nu_0}\right)^{-0.5} + \left(\frac{\nu}{\nu_0}\right)^{-3}}, \quad (2)$$

where α and ν_0 are free parameters. The MIR fit is phenomenological and so it is not characterized by specific values for the dust temperature range, orientation, torus size, or optical depth. We refer to this component henceforth as the "AGN" component. We emphasize that it could represent a structure of different shape than a classical torus, such as a more spherical cocoon, or a dusty narrow-line region (NLR) or polar wind. We also do not rule out in our later discussion that some of this warm emission could be contributed by a young compact starburst.

The modified blackbody component has a fixed dust temperature and emissivity, β. With only the single ALMA data point longward of 22 μm for most sources, it is impossible to fit the long-wavelength portion of the SED using free parameters, therefore a single graybody is the best approximation. This component may represent dust heated by star formation, or dust heated by the AGN that is cooler than the "AGN component," and of course would in reality it have a wide range of dust temperatures compared to the single value used here. The fit to the MIR region of the spectrum with the AGN component varies very little as the BB component temperature is changed, because the AGN component is very well defined by the *WISE* data on the short-wavelength side. For the four sources without measured redshift we assume $z = 2$.

For the stellar luminosity and mass we use either a 100 or 600 Myr stellar population from Maraston (2005). This is constrained only by the *R*-band data point in most cases, except for the two SDSS-detected sources, and the shape of the MIR SED at the shortest wavelengths.

We have made four fits to each source, each with a different temperature for the BB component. We have allowed the temperatures to take on a wide range so that we can interpret the luminosity as arising from disk-like distributed star formation (the coolest dust temperature, 30 K), a starburst similar to those found in local LIRGs and ULIRGs (50 K) (Melbourne et al. 2012; Bendo et al. 2015), and two additional warmer temperatures that might be appropriate for very young and compact starbursts and/or for additional AGN-heated dust (Wilson et al. 2014). For β we have selected a value of 1.5, consistent with the range of values found in the literature. For the 50 K model only, we instead used a value of $\beta = 2$,

Table 4
Minimum and Maximum Model Ranges in Luminosity, Mass, SFR, and Accretion Rate ($\dot{M}$)

Parameter	AGN	BB	Total 870 μm Detected	Total-Best	BB	Total 870 μm Not Detected	Total-Best
Min. Value	W0652–2006	W0612–0622	W0652–2006	W0612–0622	W2000–2802	W0702–2808	W0702–2808
Max. Value	W1521+0017	W0439–2159	W0439–2159	W2021–2611	W0525–3225	W1702–3225	W1702–3225
Redshift	0.60–2.63	0.47–2.82	0.60–2.82	0.47–2.28	2.28–1.69	0.94–2.85	0.94 –2.85
log L ($L_\odot$)	11.58–13.61	10.89–14.17	11.71–14.24	12.07–14.15	<10.72–<13.75	<12.09–<12.46	<12.41–<13.81
SFR ($M_\odot$ yr^{-1})	…	13.5–25700	22–25700	…[a]	<9–<9800	<22–<4360	…[a]
log $M_{\rm BH}$ ($M_\odot$)[b]	7.66–9.69	…	…[c]	8.11–10.23	…	…[c]	<8.49–<9.89
$\dot{M}$ ($M_\odot$ yr^{-1})[b]	0.24–26	…	…[c]	0.7–90	…	…[c]	<1.6–<41

Notes.
[a] No star formation is present in the Total-Best model by definition, since it is designed to resemble the intrinsic AGN SEDs.
[b] $M_{\rm BH}$ and accretion rate are directly proportional to the luminosity since we have assumed a fixed Eddington ratio and accretion efficiency.
[c] Some Total = AGN + BB fits are inconsistent with a torus-like or intrinsic AGN SED shape; the Total-Best model is the preferable maximal fit for an AGN.

consistent with the largest values found in the literature, in order to illustrate that the uncertainties due to the unknown dust temperature distribution in each source far outweigh the effect of the choice of β. This may be seen by comparing the 30 K and 50 K model fits in Figure 8. We do not expect any of these fits to be unique for any of our sources; instead we use them to constrain the range of plausible AGN and starburst luminosities.

To select appropriate dust temperatures for the two warmer BB models, we ran a set of models where $T_{\rm d}$ was allowed to be a free parameter for the two sources that have *Herschel* data, and the results are shown in Figure 7-*right*, compared to the 30 and 50 K fixed-T fits in the left panels. For W1500–0649, which was fitted in the previous section with RT models, there are two plausible fits. The 50 K BB model is reasonable, although the *IRAS* 60 μm limit is slightly exceeded. This fit requires a large fraction of the FIR emission to be explained by the warm AGN component (dashed cyan line). The best fit free-$T_{\rm d}$ model has $T_{\rm d}$ = 89 K and provides a total MIR–submillimeter luminosity of $\log(L_{\rm Total}/L_\odot)$ = 13.52, and a division between the AGN and BB components of 1.17 and 2.14 × 10^{13} $L_\odot$. This is a very similar result to the RT model. For W2059–3541 a dust temperature greater than 50 K is required to match the 70 μm PACS data. The best-fit free-$T_{\rm d}$ model has $T_{\rm d}$ = 120 K, with a total MIR–submillimeter luminosity of $\log(L_{\rm bol}/L_\odot) < 13.33$ (the 870 μm measurement is a non-detection for this source), assuming $\beta = 1.5$.

For the remainder of the sample, for which free-$T_{\rm d}$ fits are insufficiently constrained, we have adopted the two dust temperature values that have fitted W1500–0649 and W2059–3541 successfully: 90 K (rounding up from 89 K) and 120 K, for the two warmest of the four BB models. The two fits with the cooler dust temperatures, 30 and 50 K, are shown in the left-hand panels of Figure 8, while the fits with the two warmer temperatures, 90 and 120 K, are shown in the right-hand panels. The results are tabulated in Table 3. Since the AGN luminosities do not vary much between the four models, we list only the minimum and maximum AGN component luminosities in columns 3 and 4 of Table 3: $L_{\rm AGN\text{-}Min}$ and $L_{\rm AGN\text{-}Max}$.

Many of the BB fits are not successful in fitting all the data points; in particular the 120 K fits exceed the *IRAS* limits for many sources. Also the stellar component is not always fitted well by the code. We have not attempted to refine the fitting procedures to improve this situation because the current optical photometry is inadequate for this purpose. Only fits judged to be acceptable are tabulated and used in the subsequent analysis.

For the two warmer BB models, the *IRAS* 60 μm limit (and occasionally the 100 μm limit) is helpful in constraining the dust temperature of the fits for many sources. Four sources fail to find a reasonable fit for the *IRAS* limits with $T_{\rm d}$ = 90 K, while for 29 sources, the *IRAS* 60 μm limit rules out the 120 K model. In one case, W1500–0649, the 120 K model is ruled out not by *IRAS* but by ALMA and *Herschel*. In some cases the low-temperature BB models fail to allow the overall model to fit the *WISE* data; these sources are better fit with one or both of the two warmer models.

We derive SFRs from the BB components of the models using the Kennicutt (1998) conversion from far-infrared luminosity to SFR:

$$\mathrm{SFR} = 4.4 \times 10^{-37} L_{\rm BB}(\mathrm{W})\ M_\odot\ \mathrm{yr}^{-1}. \quad (3)$$

The SFR results are given in Table 6, columns 3–6, for those models that achieved successful fits.

We also list in Table 3 columns 9 and 10 the minimum and maximum summed luminosity from the up to four viable $L_{\rm Total}$ (=$L_{\rm AGN} + L_{\rm BB}$) models, $L_{\rm Total\text{-}Min}$ and $L_{\rm Total\text{-}Max}$, for each source. In addition we list $L_{\rm Total\text{-}Best}$ in column 11, which represents the $L_{\rm Total}$ fit that best resembles the SED shapes of the two sources with well fitted SEDs: W1500–0649 and W2059–3541, and the Hot DOGs with well-sampled SEDs (Figure 4). The best-fit model is indicated in column 12. In some cases the best match is derived from the average of two of the $L_{\rm Total}$ models.

The luminosities derived for the AGN from the AGN model component range from $\log(L_{\rm AGN\text{-}Min}/L_\odot) = 11.58$ to $\log(L_{\rm AGN\text{-}Max}/L_\odot)$ = 13.61. We also consider a maximum AGN luminosity derived from the Total-Best models: $\log(L_{\rm Total\text{-}Best}/L_\odot)$ = 12.01–14.15. The BB component luminosity depends strongly on assumed dust temperature. Considering all acceptable fits to the SEDs for all of the 870 μm detected sources, the acceptable range in $\log(L_{\rm BB}/L_\odot)$ is 10.89–14.17, and the corresponding SFR range is 13.5–25700 $M_\odot$ yr^{-1}. The total summed AGN + BB luminosity range is $\log(L_{\rm Total}/L_\odot)$ = 11.71–14.24. These results are summarized in Table 4.

5.3. Stellar Masses

The stellar population fit can be used to constrain the host galaxy mass from the rest-frame H-band absolute magnitude of the fitted stellar component. The host galaxy mass has only a

Table 5
Masses and Accretion Rates

WISE Name	Redshift	log M_{BH} ($M_\odot$)			log M_{BH}: Kim, et al. ($M_\odot$)		Accretion Rates ($M_\odot$ yr^{-1})			Absolute *H*-Magnitude	log M_{stars} ($M_\odot$)	log M_{ISM} ($M_\odot$)	
		Min.	Max.	Total-Best	Lower	Upper	Min.	Max.	Total-Best			30 K	90 K
W0304–3108	1.54	9.09	9.24	9.44	…	…	6.52	9.20	14.50	−24.5	10.6	10.83	10.20
W0306–3353	0.78	8.27	8.31	8.61	…	…	0.99	1.08	2.18	−23.9	10.4	10.51	9.96
W0354–3308	1.37	8.78	8.80	<9.04	…	…	3.19	3.34	<5.82	−23.6	10.2	<10.52	<9.91
W0404–2436	1.26	8.66	8.71	9.19	…	…	2.42	2.72	8.14	−25.1	10.8	10.86	10.26
W0409–1837	0.67	8.81	8.82	<8.98	…	…	3.42	3.50	<5.10	−22.6	9.8	<10.44	<9.90
W0417–2816	0.94	8.03	8.09	8.55	9.06	9.72	0.57	0.65	1.87	−22.9	9.9	10.63	10.06
W0439–3159	2.82	9.52	9.53	9.78	…	…	17.54	17.95	31.56	−23.6	10.3	11.15	10.38
W0519–0813	2.05	9.09	9.10	<9.26	…	…	6.52	6.67	<9.72	>−23.1	<10.0	<10.53	<9.85
W0525–3614	1.69	8.59	8.68	<9.02	…	…	2.06	2.54	<5.58	−23.5	10.2	<10.59	<9.94
W0526–3225	1.98	9.52	9.62	10.03	…	…	17.54	22.08	56.80	−24.1	10.4	11.64	10.96
W0536–2703	1.79	9.13	9.13	9.38	…	…	7.14	7.14	12.69	−23.7	10.3	10.82	10.16
W0549–3739	1.71	8.64	8.64	9.08	…	…	2.31	2.31	6.42	>−22.7	<9.9	10.69	10.04
W0612–0622	0.47	8.11	8.12	8.51	…	…	0.68	0.70	1.71	−23.8	10.2	10.53	10.01
W0613–3407	2.18	9.28	9.28	<9.42	9.07	9.46	10.09	10.09	<14.02	>−22.6	<9.8	<10.64	<9.94
W0614–0936	…[a]	9.02	9.03	<9.25	…	…	5.55	5.68	<9.51	−22.9	<9.9	<10.64	<9.96
W0630–2120	1.44	8.60	8.65	8.90	…	…	2.11	2.37	4.17	−24.0	10.4	11.08	10.46
W0642–2728	1.34	8.44	8.44	8.74	…	…	1.46	1.46	2.88	−24.1	10.4	10.72	10.11
W0652–2006	0.60	7.66	7.67	8.20	8.85	9.61	0.24	0.25	0.84	>−21.3	<9.2	10.70	10.16
W0702–2808	0.94	8.12	8.12	<8.49	8.92	9.73	0.70	0.70	<1.64	−21.9	9.5	<10.58	<10.01
W0714–3635	0.88	7.96	7.97	8.49	9.26	9.34	0.48	0.49	1.64	−21.7	9.5	10.69	10.13
W0719–3349	1.63	8.65	8.65	9.09	…	…	2.37	2.37	6.47	−22.5	9.8	10.51	9.74
W0811–2225	1.11	8.71	8.71	<9.02	…	…	2.72	2.72	<5.56	−24.0	10.4	<10.61	<10.02
W0823–0624	1.75	9.19	9.30	<9.43	…	…	8.20	10.57	<14.23	−24.2	10.5	<10.64	<9.99
W1308–3447	1.65	9.07	9.07	9.23	…	…	6.22	6.22	9.07	−24.4	10.6	10.53	9.89
W1343–1136	2.49	9.08	9.10	9.35	…	…	6.37	6.67	11.81	−25.7	11.1	10.74	10.00
W1400–2919	1.67	9.18	9.19	<9.51	…	…	8.02	8.20	<17.22	−24.8	10.7	<10.09	<9.44
W1412–2020	1.82	9.10	9.25	9.44	…	…	6.67	9.42	14.72	>−24.7	<10.7	10.80	10.14
W1434–0235	1.92	8.97	8.97	<9.11	…	…	4.94	4.94	<6.82	−24.5	10.6	<10.34	<9.67
W1439–3725	1.19	8.37	8.37	<8.66	…	…	1.24	1.24	<2.40	>−23.2	<10.1	<10.21	<9.61
W1500–0649	1.50	9.15	9.58	9.60	…	…	7.48	20.14	21.10	>−23.2	<10.1	11.18	10.56
W1510–2203	0.95	8.68	8.69	<8.84	…	…	2.54	2.59	<3.68	>−23.1	<10.0	<10.23	<9.66
W1513–2210	2.20	9.34	9.34	9.62	…	…	11.59	11.59	22.16	>−23.9	<10.4	11.07	10.36
W1514–3411	1.09	8.52	8.56	<8.78	…	…	1.75	1.92	<3.16	>−23.6	<10.2	<10.25	<9.67
W1521+0017	2.63	9.69	9.69	9.73	…	…	25.94	25.94	28.66	>−26.1	<11.2	11.75	11.20
W1541–1144	1.58	8.89	9.02	9.09	…	…	4.11	5.55	6.48	>−23.5	<10.2	10.46	9.83
W1634–1721	2.08	8.91	8.91	<9.06	…	…	4.31	4.31	<6.14	>−25.1	<10.8	<10.31	<9.62
W1641–0548	1.84	9.02	9.17	9.38	…	…	5.55	7.83	12.66	>−26.4	<11.3	10.75	10.09
W1653–0102	2.02	9.08	9.08	<9.18	…	…	6.37	6.37	<8.00	>−25.4	<11.0	<10.28	<9.60
W1657–1740	…[a]	9.24	9.25	<9.68	…	…	9.20	9.42	<25.42	>−25.1	<10.8	<10.28	<9.60
W1702–0811	2.85	9.68	9.68	<9.89	…	…	25.35	25.35	<41.35	>−25.2	<10.9	<10.38	<9.61
W1703–0517	1.80	9.19	9.59	9.68	…	…	8.20	20.61	25.62	>−25.1	<10.8	9.92	9.16
W1707–0939	…[a]	9.06	9.12	<9.64	…	…	6.08	6.98	<23.22	>−25.1	<10.8	<10.39	<9.71
W1936–3354	2.24	9.13	9.26	9.86	…	…	7.14	9.64	38.33	>−24.5	<10.6	10.97	10.32
W1951–0420	1.58	8.88	8.91	<9.62	…	…	4.02	4.31	<21.97	>−24.9	<10.7	<10.40	<9.76
W1958–0746	1.80	9.06	9.06	<9.18	9.53	…	6.08	6.08	<8.00	>−24.7	<10.7	<10.36	<9.70
W2000–2802	2.28	8.83	8.98	<9.04	…	…	3.58	5.06	<5.81	>−23.6	<10.2	<10.36	<9.65
W2021–2611	2.44	9.05	9.59	10.23	…	…	5.94	20.61	89.96	>−25.4	<10.9	11.24	10.56
W2040–3904	…[a]	9.00	9.23	9.57	…	…	5.30	8.99	19.81	>−24.8	<10.7	11.09	10.41
W2059–3541	2.38	9.23	9.45	<9.50	9.07	9.10	8.99	14.93	<16.76	>−25.2	<10.9	<10.35	<9.62

Note.
[a] Redshift assumed to be 2 if no spectroscopic redshift available.

small dependence on the stellar population selected by the fitting code. The masses do not depend on the dust temperature assumed for the BB dust component because the optical fit is dominated by the AGN component fitted to the *WISE* data. In a few cases, a self-consistent fit could not be obtained, indicating some possible confusion in the *R*-band data point. The *H*-band absolute magnitudes are upper limits in more than half the sample since there is no *R*-band measurement or detection, therefore most of the stellar mass estimates in columns 11 and 12 of Table 5 are also upper limits. The stellar masses derived from the models range from $\log(M_{stars}/M_\odot) = 9.83$ to 11.09 for *R*-band detected sources. The upper limits ranges from $\log(M_{stars}/M_\odot) < 9.82$ to <11.34.

The modeled intrinsic *H*-band absolute magnitudes and the derived stellar masses are highly uncertain and should be viewed as indicative only. We have no measurement of

Table 6
Star Formation Rates and Gas Depletion Timescales

WISE Name	Redshift	log SFR ($L_\odot$ yr^{-1})				log (Gas Depletion Time) (yr)		
		30 K	50 K	90 K	120 K	30 K	50 K	90 K
W0304–3108	1.54	1.73	2.70	3.16	…	9.10	7.81	7.04
W0306–3353	0.78	1.22	2.31	2.52	…	9.29	7.93	7.44
W0354–3308	1.37	<1.38	<2.38	<2.83	…	<9.14	<7.83	<7.08
W0404–2436	1.26	1.70	2.72	3.17	…	9.16	7.84	7.09
W0409–1837	0.67	…	<2.23	<2.64	…	…	<7.94	<7.26
W0417–2816	0.94	1.72	2.79	3.22	…	8.91	7.56	6.84
W0439–3159	2.82	2.28	3.08	3.57	4.41	8.87	7.66	6.81
W0519–0813	2.05	<1.54	<2.44	<2.92	<3.82	<8.99	<7.74	<6.93
W0525–3614	1.69	<1.53	<2.49	<2.95	<3.99	<9.06	<7.77	<6.99
W0526–3225	1.98	2.64	3.55	4.03	…	9.00	7.74	6.93
W0536–2703	1.79	…	…	3.18	…	…	…	6.98
W0549–3739	1.71	…	2.58	3.05	…	9.06	7.78	6.99
W0612–0622	0.47	1.13	2.29	2.00	…	9.40	7.99	7.57
W0613–3407	2.18	<1.67	<2.55	<3.03	<3.92	<8.97	<7.73	<6.91
W0614–0936	…[a]	<1.64	<2.55	<3.02	<3.93	<9.00	<7.74	<6.94
W0630–2120	1.44	1.96	2.95	3.41	…	9.12	7.82	7.05
W0642–2728	1.34	1.58	2.59	…	…	9.14	7.82	…
W0652–2006	0.60	1.35	2.48	…	…	9.35	7.96	…
W0702–2808	0.94	<1.34	<2.41	…	…	<9.24	<7.89	…
W0714–3635	0.88	1.42	2.50	…	…	9.27	7.91	…
W0719–3349	1.63	…	2.99	3.46	…	…	7.11	6.28
W0811–2225	1.11	…	…	<2.89	…	…	…	<7.13
W0823–0624	1.75	<1.60	<2.54	<3.00	…	<9.04	<7.77	<6.99
W1308–3447	1.65	1.46	2.42	2.89	…	9.07	7.78	7.00
W1343–1136	2.49	…	2.67	3.16	4.02	…	7.69	6.84
W1400–2919	1.67	<1.02	<1.97	…	<3.40	<9.07	<7.79	…
W1412–2020	1.82	1.76	2.69	3.16	…	9.04	7.77	6.98
W1434–0235	1.92	<1.32	<2.24	<2.71	<3.63	<9.02	<7.75	<6.96
W1439–3725	1.19	<1.03	<2.05	<2.50	…	<9.18	<7.86	<7.11
W1500–0649	1.50	…	3.08	3.57	…	…	7.79	6.99
W1510–2203	0.95	<0.98	<2.05	<2.47	…	<9.25	<7.90	<7.19
W1513–2210	2.20	2.10	2.98	3.46	…	8.97	7.72	6.90
W1514–3411	1.09	<1.05	<2.10	<2.53	…	<9.20	<7.86	<7.14
W1521+0017	2.63	…	…	2.87	…	…	…	8.33
W1541–1144	1.58	1.37	2.34	2.81	…	9.09	7.80	7.02
W1634–1721	2.08	<1.32	<2.22	<2.70	<3.60	<8.99	<7.73	<6.92
W1641–0548	1.84	…	2.65	3.12	…	…	7.76	6.97
W1653–0102	2.02	<1.28	<2.18	<2.65	<3.55	<9.00	<7.75	<6.95
W1657–1740	…[a]	<1.27	<2.18	<2.66	<3.56	<9.01	<7.75	<6.94
W1702–0811	2.85	<1.52	<2.31	…	<3.64	<8.86	<7.66	…
W1703–0517	1.80	1.36	2.29	2.72	3.69	8.56	7.23	6.44
W1707–0939	…[a]	<1.39	<2.30	<2.78	<3.67	<9.00	<7.74	<6.93
W1936–3354	2.24	1.69	2.56	…	3.93	9.28	8.08	…
W1951–0420	1.58	<1.32	<2.29	…	>5.41	<9.08	<7.79	…
W1958–0746	1.80	<1.32	<2.25	<2.72	<3.65	<9.04	<7.77	<6.98
W2000–2802	2.28	<0.96	<1.83	<2.31	<3.20	<9.40	<8.16	<7.34
W2021–2611	2.44	2.09	2.92	…	4.28	9.15	7.97	0.00
W2040–3904	…[a]	2.09	3.00	3.47	…	9.00	6.94	…
W2059–3541	2.38	…	…	<2.70	<3.11	…	…	<6.92

Note.
[a] $z = 2$ assumed for sources without a spectroscopic redshift.

extinction for the optical or *WISE* data points, and no color information to help constrain the stellar populations. We also have little information on morphology, and therefore on the stellar components included in the flux density. It is also possible that some of the emission is scattered AGN light. The fitting of the stellar component will be greatly improved by the use of the J and K_s data, therefore we limit discussion of these results in this paper.

5.4. Radio Powers, Radio Loudness and the q Parameter

The rest-frame 3 GHz radio powers in column 13 of Table 3 are found to lie in the range $\log(P_{3\mathrm{GHz}}/\mathrm{W\ Hz^{-1}}) = 24.74$–$27.33$, adopting a power-law spectral index $\alpha = -1.0$ ($f_\nu \propto \nu^\alpha$) for the k-correction to 3 GHz rest frequency. The median/mean value is 25.97/26.05. We also list the rest-frame (i.e., k-corrected) $q_{22} = \log(f_{22\,\mu\mathrm{m}}/f_{1.4\,\mathrm{GHz}})$ values in column 14. The MIR k-correction for q obviously

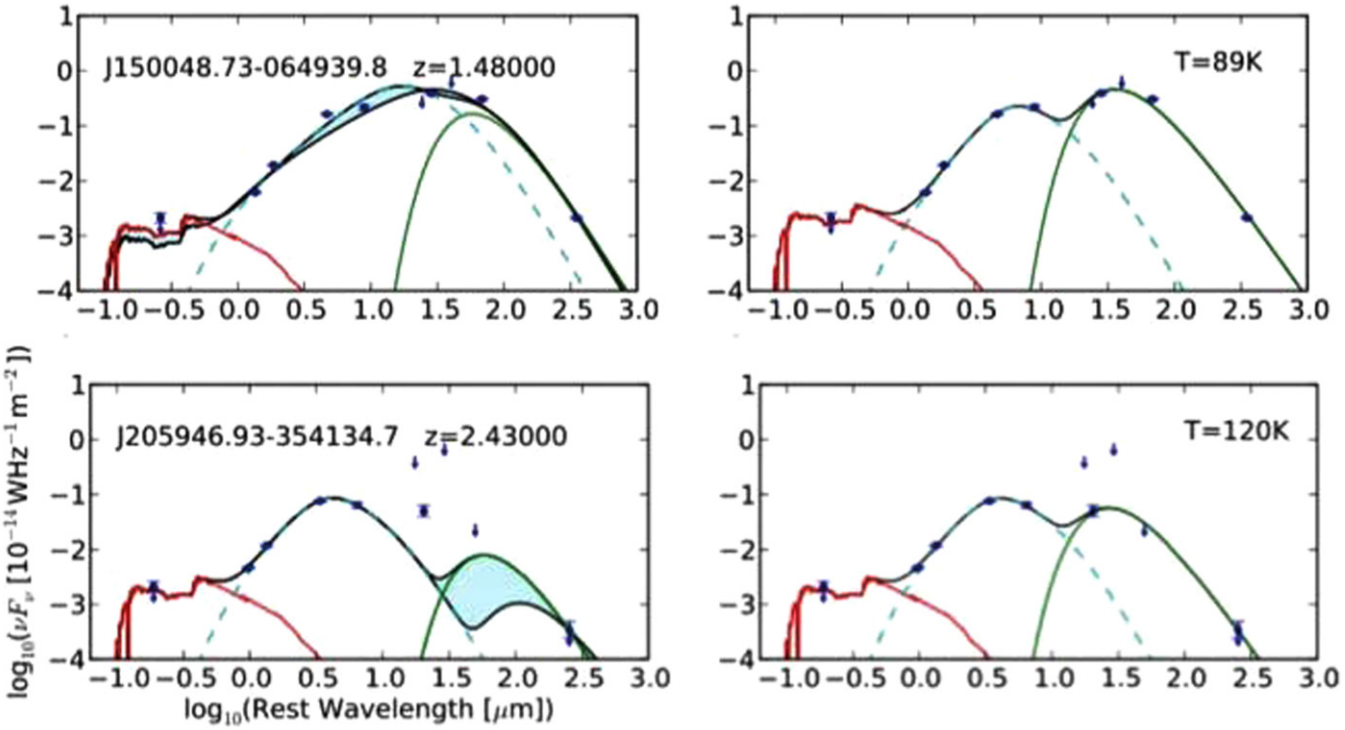

Figure 7. SED models for the two sources for which we have sufficient data near the peak of the SED, from *Herschel*, to obtain well constrained fits across the MIR and FIR: W1500–0649 and W2059–3541. "AGN" (dashed cyan line); modified blackbody "BB" dust component (green lines); stellar population (red lines); summed model (black line). For the AGN and stellar components, and for the total fits, only one fit is shown in each panel, for clarity. The ALMA data point is the rightmost point, and the limits near the peak of the cool component are 60 and 100 μm *IRAS* data. Left: models with $T_d = 50$ K, $\beta = 2$ (upper) and $T_d = 30$ K, $\beta = 1.5$ (lower). Right: models in which the temperature of the BB dust component is allowed to float, for these two sources only, with $\beta = 1.5$.

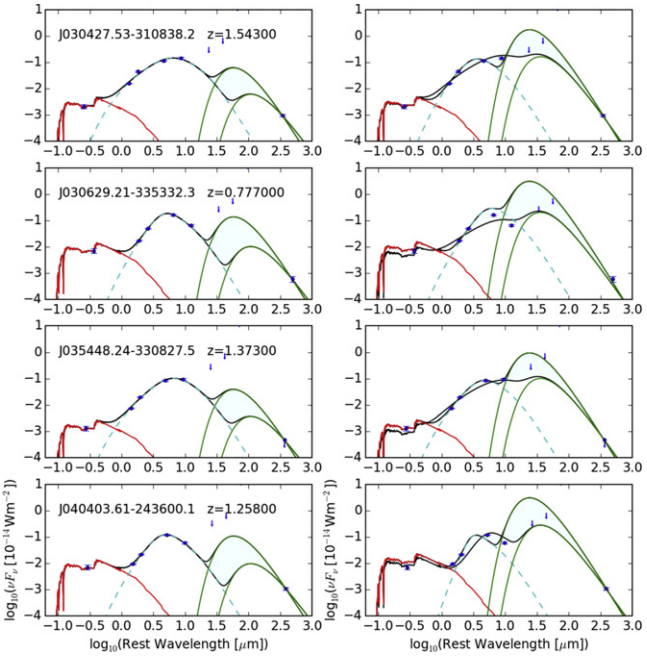

Figure 8. SED models for each source: data and fits as in Figure 7. Many of the BB models do not provide good fits, and these are not considered further in our analysis. In some cases no consistent fit is found for the stellar component. Left: models with $T_d = 50$ K, $\beta = 2$ (upper) and $T_d = 30$ K, $\beta = 1.5$ (lower). Right: models with 90 K (lower) and 120 K (upper), with $\beta = 1.5$; temperature choices based on the results for W1500–0649 and W2059–3541 in Figure 7.

depends strongly on the assumed rest-frame SED. In our situation this is particularly tricky because the unknown depth of the silicate feature will affect the observed f_{22} flux density strongly at redshifts near 1.5 (e.g., see Figure 3). We have used the QSO2 ("Torus") template of Polletta et al. (2007) because it was successfully fitted by them (their Figure 9) to a very red, Compton-thick, *Spitzer*-selected obscured QSO that is similar in NIR–MIR spectral shape to our sources. To this we have grafted on the silicate absorption feature from the Arp 220 template of Polletta et al. (2007). We also derived the *k*-correction without the added silicate feature. All of the templates have been convolved with the *WISE* 22 μm filter as a function of redshift by Polletta et al. (2007). Our quasars have comparable *k*-corrected q_{22} values to the most radio-powerful and most radio-loud sources in the large *Spitzer Subaru* X-ray Deep Field sample of Ibar et al. (2008), and all of our sources would be considered to be moderately to very radio-loud after the *k*-correction, based on this criterion. This is the case even if the large silicate optical depth is omitted from the template. This conclusion is also apparent from Figure 4, in which our quasars lie between the radio-quiet (RQ) and radio-loud (RL) quasar templates, when normalized at 4.6 μm rest.

5.5. BH Masses and Accretion Rates

Lacking a high quality spectroscopic indicator of BH masses such as the Mg II emission line width, we derive BH masses and accretion rates from the AGN luminosities. These three parameters are therefore directly proportional to each other in

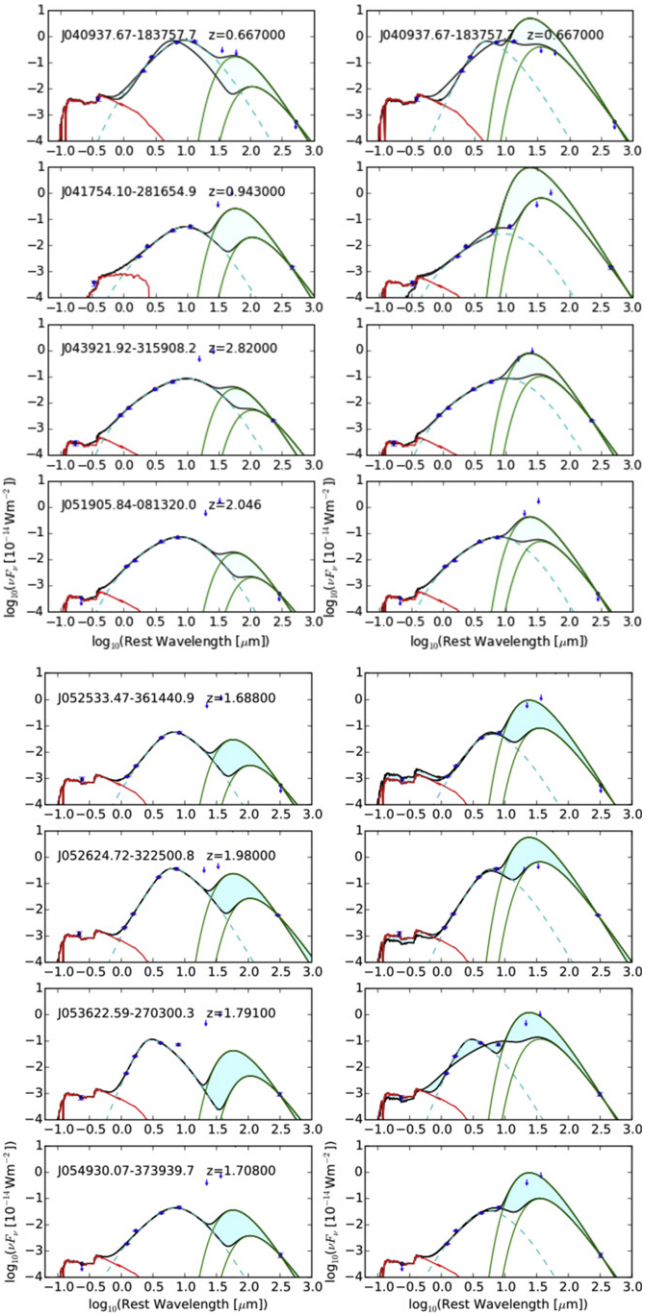

Figure 8. (Continued.)

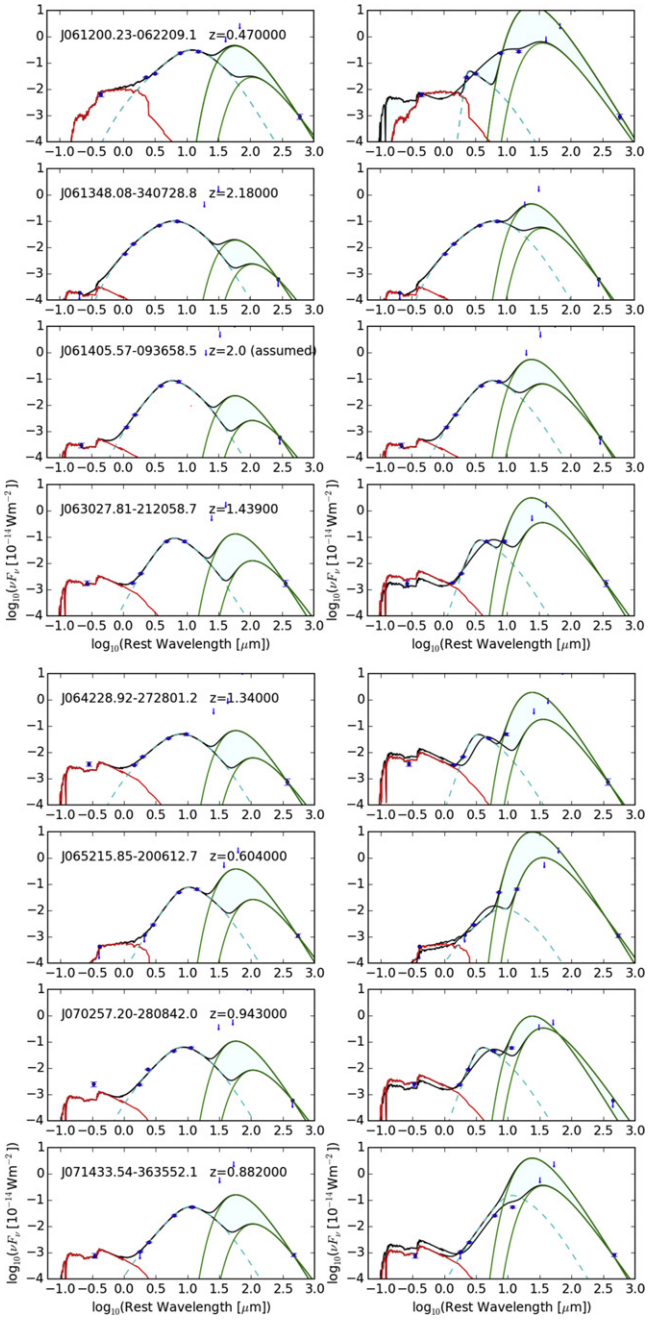

Figure 8. (Continued.)

this work. We assume an Eddington ratio, $\lambda_{\rm Edd}$, of 0.25, which is typical of $z \sim 2$ quasars (Kormendy & Ho 2013):

$$L_{\rm Edd} = \left(4\pi G m_p c/\sigma_{\rm T}\right) M_{\rm BH} = 3.3 \times 10^4\ M_{\rm BH}. \quad (4)$$

We assume a covering factor of unity and spherical symmetry, consistent with late-stage mergers with heavily obscured nuclei. The covering factor cannot actually be this high in most sources, since emission lines from the NLR are visible in many cases; therefore our AGN luminosities and BH masses may be underestimates due to missing emission in the X-ray to optical range which is not absorbed by the dust. We present the results in Table 5, columns 3–5, using our $L_{\rm AGN\text{-}Min}$, $L_{\rm AGN\text{-}Max}$, and $L_{\rm Total\text{-}Best}$ estimators. The median/mean BH mass values are 1.0/1.15, 1.07/1.45, and 1.55/2.75 $\times$ 10^9 $M_\odot$ respectively. In columns 6 and 7 we also list the BH masses derived by Kim et al. (2013), based on the [O III]λ 5007 Å line luminosity.

The accretion rates are derived from the AGN luminosities assuming an efficiency for the conversion of matter into radiant energy of $\epsilon = 0.1$ (Heckman & Best 2014):

$$L_{\rm bol} = \epsilon \dot{M} c^2. \quad (5)$$

The rates are listed in columns 8–10 of Table 5, and range from 0.24 to 25.3 $M_\odot\,{\rm yr}^{-1}$, with median/mean values of 6.1/5.6, 7.6/6.2, and 14.5/9.1 $M_\odot\,{\rm yr}^{-1}$ respectively for the AGN-Min, AGN-Max, and Total-Best values. The overall ranges in BH mass and accretion rate are listed in Table 4.

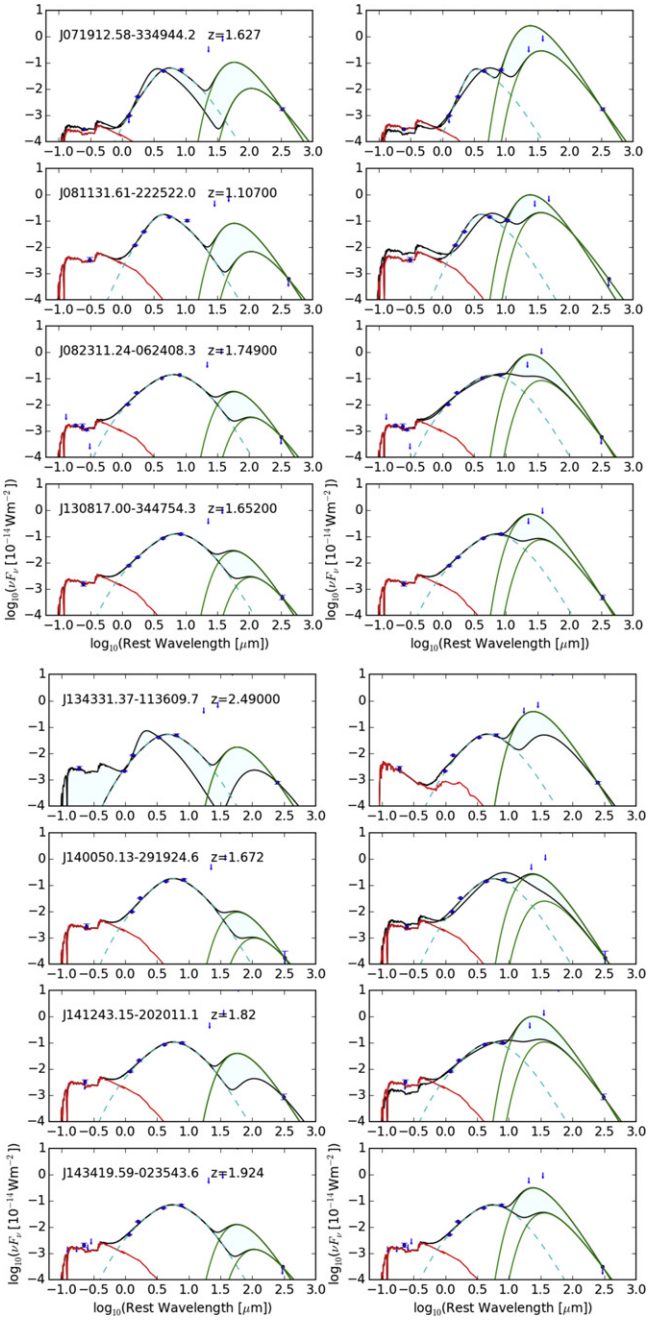

Figure 8. (Continued.)

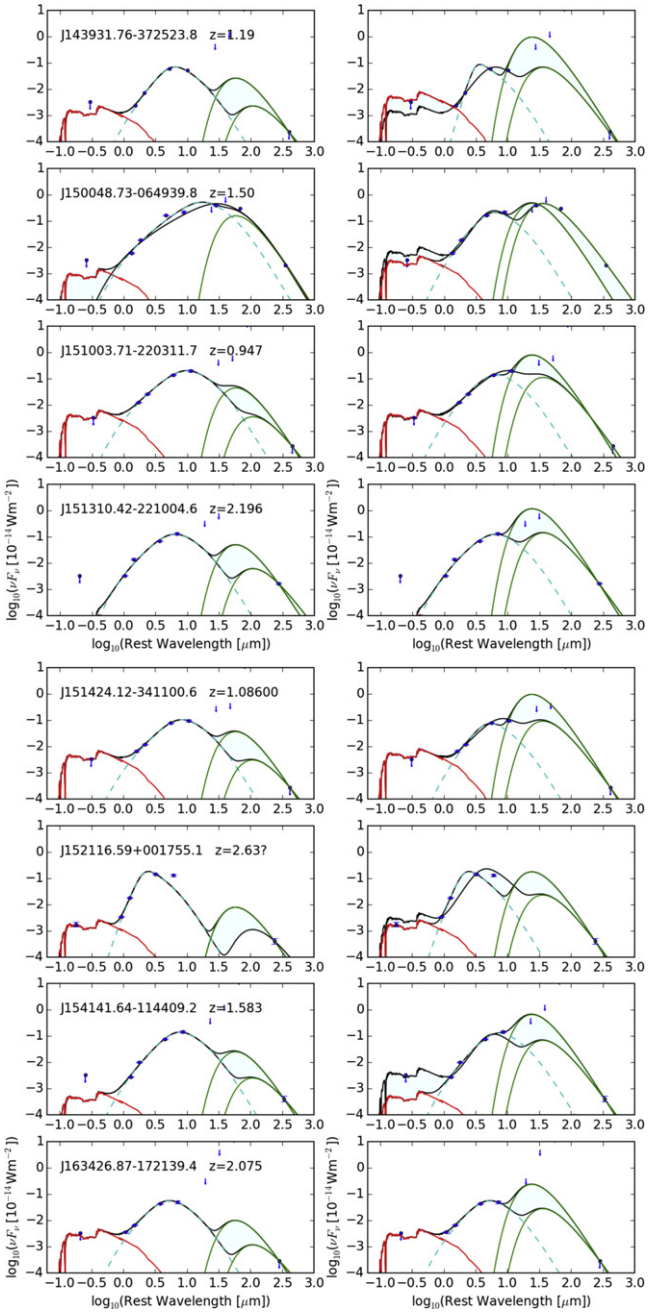

Figure 8. (Continued.)

6. DISCUSSION

Our goals are to search for the most luminous obscured quasars at redshifts ∼1–3, the peak epoch of massive BH building, which are in the process of quenching star formation, and to investigate the role of radio jets in that process. We are specifically interested in the kinetic role of moderate to high power jets on the ISM within the galaxy host, while the AGN is still accreting strongly in "quasar-mode." This is in contrast to the role of jets in typical "radio-mode" AGNs, which are thought to be accreting at low rates and to have a role in maintaining galaxies free of infalling gas. As outlined in Section 1, models that take the porosity of the ISM into account show that high power jets could be quite effective in a dense dusty environment, such as found in the central regions of major mergers (Wagner & Bicknell 2011; Wagner et al. 2012).

We have shown that *WISE* has found sources that are steeper (redder) in the rest-frame 1–10 μm range than most known *Spitzer*-selected red sources, including the so-called DOGs. The two other samples of very red *WISE* sources, the Hot DOGs and the WLABs (EWB12) that were selected without regard for radio emission, have extremely red rest-frame 1–10 μm SEDs which are very similar to those of our radio-selected sample. The radio-blind samples have higher average redshifts than our radio-powerful sample, probably as a result of the different *WISE*-optical color selection criteria. We attribute our ability to identify these extremely red sources to the much larger survey volume of *WISE* compared to *Spitzer*.

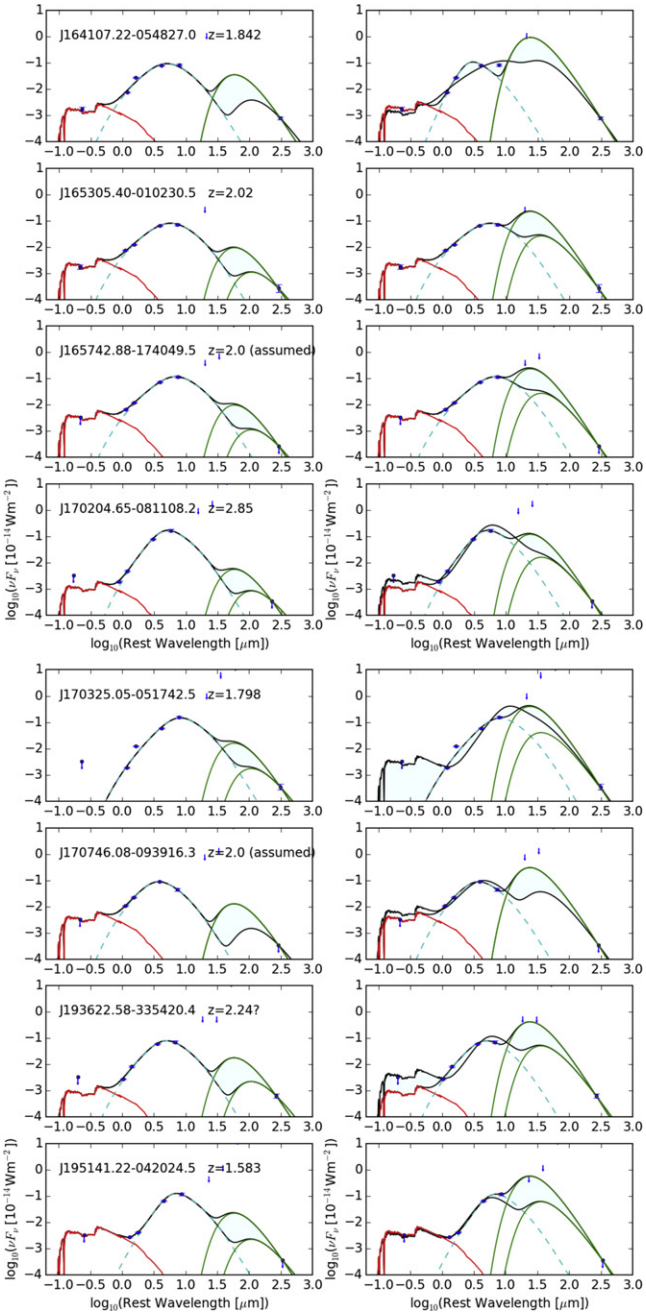

Figure 8. (Continued.)

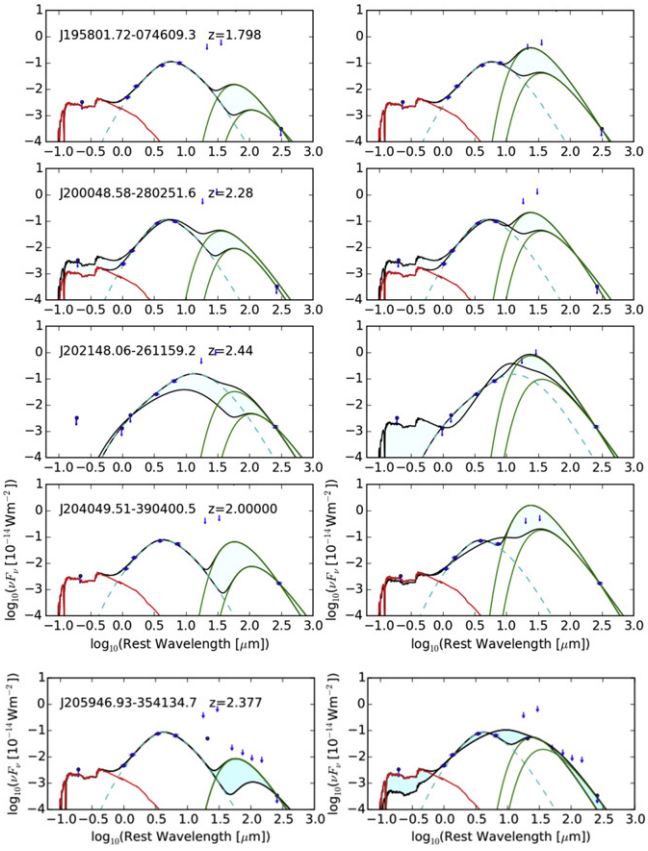

Figure 8. (Continued.)

These systems are candidate luminous quasar-mode AGNs that are highly obscured, and the radio-bright ones selected here potentially have young jet activity. Recent X-ray observations of a few Hot DOGs confirm the likelihood of highly buried AGNs (Stern et al. 2014; Pinconcelli et al. 2015). The hydrogen column for W1835+4355 was found to be $N_{\rm H} \geqslant 10^{23}\,{\rm cm}^{-2}$ by Pinconcelli et al. (2015).

We also find that the *WISE*-NVSS-ALMA sample sources are more strongly dominated by AGNs than the *Spitzer* DOGs. SFRs of hundreds up to a few thousand $M_{\odot}\ {\rm yr}^{-1}$ could also be present in some of the systems, although the IR–submillimeter SEDs of some of the ALMA sources, in particular those with only upper limits at 345 GHz, may be consistent with the AGN torus model in Figure 4 without any SF contribution. Therefore these sources are indeed objects in which it is likely that the accretion rates are still very high but the SFRs are low *relative to the accretion power*, and could thus be ideal sources for investigating recent and ongoing quenching by jet-powered AGN feedback.

Some of our systems could be HERGs seen at high inclination through an optically thick torus, and it is possible that we have included some with lobes that are unresolved by the 45″ NVSS beam. We will show in the next paper (Carol J. Lonsdale et al. 2015, in preparation) that our 8–12 GHz VLA data rule out this scenario for most sources, although a small subset of the VLA sample of 156 red obscured quasars does indeed turn out to have large (several Mpc scale) double lobes (∼7%). Another small percentage shows evidence of small-scale double lobes on scales ∼2–10 kpc.

6.1. The AGN-heated Source

In this work we have derived a range in the plausible AGN luminosities depending on whether we assume that any of the far-infrared luminosity component is AGN-heated:

$$L_{\rm bol,\,AGN} = L_{\rm AGN,\,MIR} + f_{\rm AGN} L_{\rm BB}$$

where $L_{\rm bol,AGN}$ is the bolometric luminosity of the AGN, $L_{\rm AGN,\,MIR}$ is the MIR AGN luminosity from the fit to Equation (2), $f_{\rm AGN}$ is the fraction of the far-infrared emission contributed by the AGNs and $L_{\rm BB}$ is the far-infrared luminosity. $f_{\rm AGN}$ is assumed to be 0 for the $L_{\rm AGN}$ models and to be 1 for the scenario in which we assume that $L_{\rm Total\text{-}Best}$ is completely AGN-powered. The warm AGN component luminosity is very

insensitive to the dust temperature of the BB component, due to the strong constraints placed on the AGN model shape by the four *WISE* data points. The range of values for the ratio of the maximum plausible AGN luminosity to the minimum estimate is $1.1 < L_{\rm Total\text{-}Best}/L_{\rm AGN\text{-}Min} < 5.5$, with a median value of 2.0.

We have assumed a covering factor of warm (~300 K) dust that emits in the MIR, $\Omega_{\rm WD}$:

$$L_{\rm bol,\,AGN} = L_{\rm AGN,\,MIR}/\Omega_{\rm WD}$$

of unity and spherical symmetry, consistent with late-stage mergers with heavily obscured nuclei. This may not be a valid assumption, in which case we may have underestimated the AGN luminosities and BH masses. In particular, narrow emission lines photoionized by the AGNs are seen in many cases, therefore these luminosity estimators may be excluding flux emitted by the AGNs that does not intercept the dusty structure. A further complication is that the covering factor of the cold (~50 K) dust is likely to be different from that of the hot dust, and its optical depth to the MIR emission is unknown.

An added complication is the possibility that a non-spherical source emits non-isotropically because it is optically thick, as is often the case for torus models (e.g., Efstathiou et al. 2013). In that case a further correction for anisotropy is required, and this depends on the particular torus model and also on the inclination of the torus. Generally speaking, for edge-on viewing the luminosity will be underestimated whereas for face-on viewing it may be overestimated. Face-on viewing is ruled out by the red MIR–optical SEDs and therefore we can conclude that $L_{\rm AGN,MIR}$ provides a firm lower limit to the bolometric luminosity of the AGNs.

Support for the high covering factor interpretation for most of our *WISE*-NVSS-ALMA sample comes from the overall relative numbers of obscured and unobscured AGNs among the highest luminosity radiative=mode AGNs at high redshift ($z \sim 1$–3), which are roughly equal (Assef et al. 2015; Lacy et al. 2015; Tsai et al. 2015). Taken at face value this would imply an average covering fraction of ~50%, if these populations differ only by orientation (ignoring the differing selection functions for type 1 and type 2 AGNs, Elitzur 2012).

6.1.1. A Torus?

Although we have commented above on the likelihood that the covering factor may be lower than 1.0 for many sources, it might be questionable to conclude that a classical smooth torus could be responsible for the very high luminosities found for some sources, because they would require very large tori (several hundred pc to over a kpc in diameter), especially if the $L_{\rm Total\text{-}Best}$ values are interpreted as fully AGN-powered. Such large thin structures would be unstable. A clumpy torus would be more plausible, as it could achieve a wider range of dust temperatures than a smooth torus of the same diameter.

A torus-like structure would imply that a large fraction of the total AGN luminosity escapes dust absorption and would be easily visible at optical wavelengths. Since the line-of-sight optical continuum emission is very faint compared to type 1 AGNs (Figure 4) the tori would all have to be inclined closely to our line of sight. Our selection function of course has favored the selection of highly obscured systems, and we do indeed find a fraction of our sample to have (small) double radio lobes in the plane of the sky (Section 5.4), as might be expected for a radio quasar or radio galaxy interpreted as viewed through an edge-on disk in the standard unification picture. The majority of our sample does not display extended radio lobes, however.

6.1.2. Extended NLRs, Polar Winds, and Lyα Blobs

High-resolution observations of nearby low-luminosity AGNs show that the MIR emission can lie in the polar direction and may be associated with NLR clouds or with thermal winds from the AGNs (Zhang et al. 2013 and references therein). It is also known that a significant fraction of FRII radio AGNs have extended emission line regions (EELRs) up to tens of kpc in size (Fu & Stockton 2007), which are outflowing (Shih & Stockton 2014). The CSS sources, which are younger versions of the FRIIs, have smaller EELRs that are better aligned with the radio structures than they are in FRIIs (Axon et al. 2000). Therefore it is possible that some of the MIR emission in our sample is associated with NLR or EELR clouds that are heated by the central AGN, or shock-heated by the radio jet interactions (Mullaney et al. 2013). Efstathiou et al. (2013) have found that a dusty NLR component is needed to fit the MIR–FIR SED of the hyperluminous galaxy IRAS10214+4724 at $z = 2.285$.

Bridge et al. (2013) have discovered that a subset of the Hot DOGs that have extended faint optical emission also possess Lyman alpha Blobs (LABs; defined to have Lyα emission extended on scales >30 kpc). The *WISE* LABs are non-symmetric and there is evidence for large outflow velocities. The presence of extended ionized gas suggests significant shock heating or that a significant fraction of the nuclear ionizing radiation must be able to find its way out of the galaxy, as in the radio galaxy EELRs, even in these highly obscured MIR-dominated systems. Few of our sources currently have spectra that cover Lyα. W0613–3407 has Lyα extended spatially on a scale of 3″, so qualifies as an LAB by the size definition. W1343–1136 appears to also have extended emission (about 2.″5; 25 kpc) but to just miss the usual LAB definition of >30 kpc. Although it remains to be seen whether a large fraction of our *WISE*-NVSS-ALMA sources possess LABs, we have some evidence that some of them possess broad forbidden emission lines that might indicate substantial outflows. Kim et al. (2013) find that the [O III] lines are exceptionally broad for six of our quasars, with full width at half maximum ~1300–2100 km s^{-1}, significantly larger than that of typical distant quasars.

6.2. Star Formation

The contribution to the 1–1000 μm luminosity from star formation has larger overall uncertainty than the AGN contribution because star formation can produce a larger range in observed dust temperature, varying by ~2 dex between the viable 30 to 120 K BB models (Table 6, columns 4–6). The maximum star formation luminosity, $L_{\rm BB\text{-}Max}$, is comparable to the the AGN luminosity estimators, while the minimum starburst luminosity, coming from the 30 K model in all but one case, can be well over an order of magnitude smaller than the AGN luminosity. A minimum SFR of 0 is also possible if $L_{\rm Total\text{-}Best}$ is interpreted as completely AGN-powered.

If we adopt 50 K dust for the BB component, the SFRs lie between ~200 and 3500 $M_\odot$ yr^{-1}. The lower values are consistent with main-sequence galaxies at these redshifts while

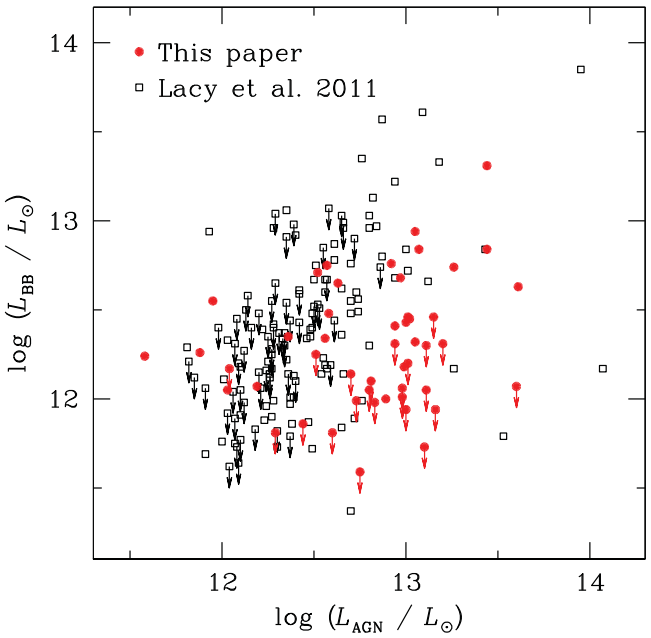

Figure 9. Comparison of the *Spitzer*-selected sample of Lacy11 with our sample in the L_{AGN} vs. L_{BB} plane. For this figure we show the BB luminosity from our 50 K model to match the method used by Lacy11.

the higher values may require a starburst (Delvecchio et al. 2015).

Our RT modeling of our best observed source favored the presence of a young (10–15 Myr), presumably compact, starburst contributing about 50% of the 1–1000 μm luminosity. Compact starbursts have been investigated in several local galaxies. The nuclear structures around the twin nuclei of Arp 220 are thought to be powered by compact starbursts with relatively high dust temperatures (over 100 K) and to be highly optically thick out to $\gg$100 μm (Wilson et al. 2014; Barcos-Munoz et al. 2015; Scoville et al. 2015). Tsai et al. (2015) have considered in more detail the possibility that a compact starburst could contribute a significant luminosity to their most luminous Hot DOGs, those with $L_{bol} > 10^{14} L_\odot$. Using He 2–10 as a local analog and the STARBURST99 code (Leitherer & Chen 2010), they find SFRs $>5 \times 10^3$ $M_\odot$ yr^{-1} for the conservative case of a top heavy IMF.

Tsai et al. (2015) conclude that there is insufficient CO in these systems to support very large amounts of star formation. In our case we find mean ISM masses of between $\sim$2 and 9 $\times$ 10^{10} $M_\odot$, depending on the assumed dust temperature. For the range of estimated SFRs across our models the gas would be depleted in $\sim$2 Myr–2 Gyr. The lower depletion times (corresponding to the higher SFRs) are not insupportable, in the scenario of a late-stage, violent, gas-rich merger. Therefore it is quite possible that a vigorous starburst is present in some of our systems, and that a compact young starburst may contribute to the warmest dust emission.

6.3. High Accretion Rates Relative to Star Formation

In Figure 9 we plot $L_{AGN\text{-}Min}$ versus $L_{BB\text{-}50\,K}$: no correlation is apparent. We compare our sample to the radio-quiet *Spitzer*-IRAC-selected quasar sample of Lacy et al. (2011, Lacy11), for which fits have been done using the same formalism as here. The Lacy11 sample has a wider range in mid-IR color selection than our sample, including Type 1 quasars, reddened Type 1 quasars and Type 2 quasars, and is therefore representative of the IR-bright AGN population as a whole. There is some evidence that the heavily obscured quasars in our sample have similar far-infrared luminosities to the Lacy11 sample, i.e., similar SFRs, but systematically higher AGN luminosity. This is consistent with them being in a phase of systematically higher accretion rate relative to star formation.

6.4. ISM Masses

The masses of the BH, the ISM, and the stellar component are tabulated in Table 5. The ISM mass is directly proportional to the 870 μm luminosity, but depends much less strongly on dust temperature than do L_{BB} and SFR.

We found in Section 5.1 that the ISM masses are comparable to those of the "IR-bright" high-redshift sources in the COSMOS field (Scoville et al. 2014). We can also compare our sample to the compilation of all known molecular masses for $z > 1$ systems of Carilii & Walter (2013), their Figure 9. Assuming a CO to H_2 conversion factor appropriate for starbursts (Downes & Solomon 1998; Bolatto et al. 2013) of $\alpha_{CO} \sim 0.8$ $M_\odot$/(K km s^{-1} pc^2), and assuming 50% of the gaseous ISM is in molecular form (Carilii & Walter 2013), our median detected ISM mass implies a median molecular gas mass of 2.95×10^{10} $M_\odot$ and a median CO line luminosity of 3.7×10^{10} K km s^{-1} pc^2. This lies at about the 80th percentile of the high-redshift QSOs in Figure 9 of Carilii & Walter (2013), and about the 50th percentile of the SMGs. It is lower than four of the RGs in this figure and comparable to the other two.

In summary, if we assume no contribution to the measured ALMA fluxes from non-thermal synchrotron emission, we find that the implied ISM masses are quite high, comparable to those of typical "IR-bright" star-forming systems in the COSMOS field at these redshifts, to the most gas-rich galaxies in the local CO survey of Leroy et al. (2009), and consistent with the large CO masses of $z > 1$ QSOs, SMGs, and RGs. This gas and dust could exist in nuclear, AGN-heated structures, or it could be powered by star formation somewhere within the host system.

6.5. BH Masses

The BH mass estimates derived by Kim et al. (2013) for three of the six quasars with available [O III] λ5007 Å line luminosities are significantly larger than the values derived from our MIR data. Our masses may be underestimated due to extreme extinction in the MIR (although we might expect to recover such dust-absorbed energy in the FIR–submillimeter), and our assumption of $\sim$100% covering factor may be incorrect. Another possibility is that the [O III] line strengths of Kim et al. (2013) are boosted by shocks and outflows. We will address the relationship between L_{MIR} and $L_{[O\,III]}$ for these systems (cf. Mullaney et al. 2013) in a forthcoming paper presenting the spectroscopy.

6.6. Nature of the Radio Sources

We will address the morphology of the radio sources in our paper presenting the VLA results, where we will show that the majority of the sample are compact on $\sim$1–3 kpc scales. The rest-frame 3 GHz radio powers lie in the range log ($P_{3.0\ GHz}$ /W Hz^{-1}) = 24.74–27.33. The radio power of both RQ and RL systems evolves with redshift (Best et al. 2014), and some

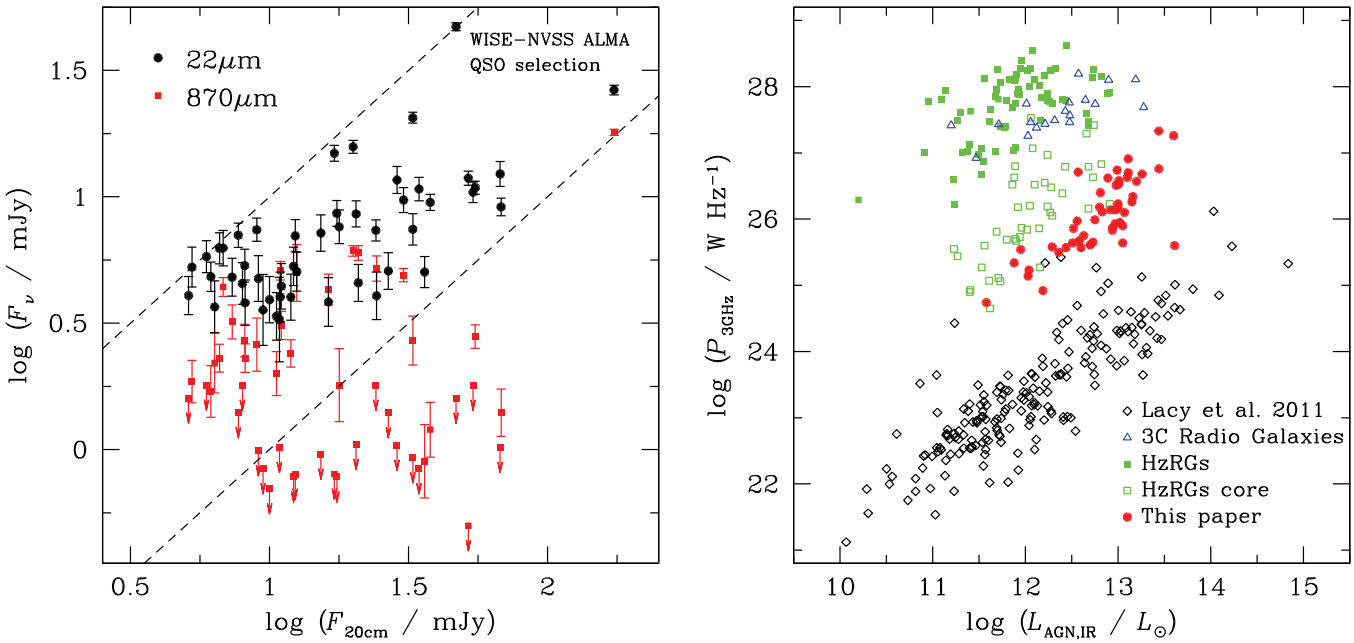

Figure 10. Left: selection criteria for the ALMA quasar sample at 22 μm and 20 cm. An apparent weak correlation between 22 μm and 20 cm flux density may be due to the selection boundaries (dashed lines). Also shown is the 870 μm flux density vs. 20 cm flux density, showing no trend. Right: AGN luminosity vs. radio power for our *WISE* sample and for the HzRGs of De Breuck et al. (2010) (both total emission and core emission), the 3C quasars from Cleary et al. (2007), and the MIR-selected AGNs of Lacy11.

radio sources at $z = 1$–3 with radio powers in this range are found to be radio-quiet based on the 24 μm q value, $q_{24} = \log(f_{24\mu m}/f_{20\,cm})$ (Simpson et al. 2012). Our sources have values of q_{22} that are significantly too low for them to be considered radio-quiet by this criterion.

In Figure 10-*right* we compare $L_{\rm AGN\text{-}Min}$ with $P_{\rm Radio\text{-}3\ GHz}$, and also include the high-redshift ($1 < z < 5.2$) radio galaxy (HzRG) sample of De Breuck et al. (2010) and the 3C radio galaxy sample of Cleary et al. (2007) at $0.4 < z < 1.2$. For the HzRG sample we also include the estimated core flux, using the 20 GHz core fractions given by De Breuck et al. (2010) and assuming that the same fraction is appropriate at 3 GHz. There is a large disparity between our sample, the Lacy11 sample, and the two high-redshift samples. The HzRGs and 3C RGs have 2–3 orders of magnitude more radio power than our sample, for a given mid-IR AGN luminosity, which is expected given that the power of the HzRGs is dominated by the extended lobes. The core radio powers for the classical HzRGs have a similar range to our sample but our sources are significantly more luminous in the infrared, consistent with a higher accretion rate. The radio-blind MIR-selected sample of Lacy11 has on average 2–3 orders of magnitude less radio power than our sample, as expected for an RQ-dominated sample.

All four samples in this figure display an apparent correlation between $L_{\rm AGN}$ and $P_{\rm Radio\text{-}3\ GHz}$. Given the rarity of these sources and the large redshift range involved, the correlation for our sample may be an artifact of Malmquist bias resulting from the 22 μm and the 1.4 GHz flux density thresholds. We show in Figure 10-*left* that there exists an apparent correlation between 22 μm and 20 cm flux density that may be caused by the limited dynamic range in the flux ratio selection thresholds for the *WISE*-NVSS-ALMA sample: $-1 < \log(f_{22\,\mu m}/f_{20\,cm}) < 0$ (dashed lines). Therefore the apparent correlation seen between $L_{\rm AGN}$ and $P_{\rm Radio\text{-}3\ GHz}$ in Figure 10-*right* may not be real, at least for our sample.

7. CONCLUSIONS

We have selected a sample of extremely red, luminous, RP sources in the $0.5 < z < 3$ redshift range using *WISE* MIR colors and the NVSS and FIRST 20 cm radio surveys. We present ALMA 870 μm photometry for 49 southern sources from the total sample of 156 red sources, and redshifts for 45 of them from a combination of optical and near-infrared spectroscopy. JCMT imaging at 850 μm has been presented for 30 of the northern sample by Jones et al. (2015). Combined, 30 sources have a detection at 850 or 870 μm, 25 of them with a known redshift. We also have *R*-band imaging for 27 sources, *Herschel* photometry for 15 sources, including two of the ALMA sample, and CSO 350 μm data four additional sources, including two from the ALMA sample.

Having compared the SEDs of the red *WISE*-selected sources with other samples and template SEDs, we conclude that the rest-frame MIR–submillimeter SEDs of our *WISE*-NVSS sources are dominated by AGN emission in the MIR. They have extremely red optical–MIR colors and high bolometric luminosities in the ULIRG and HyLIRG regime, in some cases approaching or exceeding $10^{14}\,L_\odot$. They are redder in the NIR–MIR than previous samples selected from *Spitzer* surveys, including almost all of the *Spitzer* DOGs. They also display systematically warmer overall MIR–submillimeter SEDs, and probably have higher levels of accretion, relative to star formation, than the DOGs. BH mass estimates for our sample are $7.7 < \log(M_{\rm BH}/M_\odot) < 10.2$. We conclude that these sources are best labeled as obscured RP QSOs. The rest-frame 3 GHz radio powers are $24.7 < \log(P_{3.0\,GHz}/{\rm W\ Hz^{-1}}) < 27.3$, and all sources are radio-intermediate or radio-loud. The ability of *WISE* to find this rare and unique sample is due to the large volume accessible to *WISE*.

Our best constrained source has RT solutions with approximately equal contributions for an obscured AGN and a young (10–15 Myr) compact starburst. Simpler two-component fits to the whole sample find that the SFRs of the sample could be in the range of hundreds to thousands of solar masses per year, but it also possible to fit a significant fraction of the ALMA data for some sources with a centrally heated dusty structure, in which case most of the entire bolometric luminosity could be attributed to the obscured AGN. In that scenario it is likely that the emission is dominated by a small, high covering factor cocoon and/or an extended NLR.

Our sample is similar in MIR selection method to Eisenhardt et al. (2012), Wu et al. (2012), and Bridge et al. (2013), who did not use radio flux density as a selection criterion. Their Hot DOG samples exhibit similar SED shapes to our radio-selected sample. The MIR SEDs of the EWB12 samples may be steeper on average than those of our radio-selected sample, but this may be due to different selection effects between the MIR–optical color selection criteria for the two samples, resulting in an average higher redshift for the radio-blind sample.

This paper makes use of the following ALMA data: ADS/JAO.ALMA#2011.0.00397.S. ALMA is a partnership of ESO (representing its member states), NSF (USA), and NINS (Japan), together with NRC (Canada), NSC and ASIAA (Taiwan), and KASI (Republic of Korea), in cooperation with the Republic of Chile. The Joint ALMA Observatory is operated by ESO, AUI/NRAO, and NAOJ. This publication makes use of data products from the *Wide-field Infrared Survey Explorer*, which is a joint project of the University of California, Los Angeles, and the Jet Propulsion Laboratory/California Institute of Technology, funded by the National Aeronautics and Space Administration. This work is based on observations made with the Caltech Submillimeter Observatory, which is operated by the California Institute of Technology under funding from the National Science Foundation, contract AST 90-15755. This paper uses data from SDSS (DR 8). Funding for SDSS-III has been provided by the Alfred P. Sloan Foundation, the Participating Institutions, the National Science Foundation, and the U.S. Department of Energy Office of Science. The SDSS-III web site is http://www.sdss3.org/. RJA was supported by Gemini-CONICYT grant number 32120009. We thank the anonymous referee for comments that helped improve the paper. The National Radio Astronomy Observatory is a facility of the National Science Foundation operated under cooperative agreement by Associated Universities, Inc.

Facilities: WISE, VLA, ALMA, CTIO (SOAR–Goodman), Palomar 200 inch, VLT, *Herschel*, CSO, *Magellan*.

REFERENCES

Aalto, S., Garcia-Burillo, S., Muller, S., et al. 2015, A&A, 574, 85
Appleton, P. N., Fadda, D. T., Marleau, F. R., et al. 2004, ApJS, 154, 147
Appleton, P. N., Xu, K., Reach, W., et al. 2006, ApJS, 639, L51
Archibald, E. N., Dunlop, J. S., Hughes, D. H., et al. 2001, MNRAS, 323, 417
Ashby, M. L. N., Stern, D., Brodwin, M., et al. 2009, ApJ, 701, 428
Ashby, R. F., Stanford, S. A., Brodwin, M., et al. 2013, ApJS, 209, 22
Assef, R., Stern, D., Kochanek, C. S., et al. 2013, ApJ, 772, 26
Assef, R. J., Eisenhardt, P. R. M., Stern, D., et al. 2015, ApJ, 804, 27
Assef, R. J., Kochanek, C. S., Brodwin, M., et al. 2010, ApJ, 713, 970
Axon, D. J., Robinson, A., Young, S., Smith, J. E., & Hough, J. H. 2000, AJ, 120, 2284
Baldwin, J. A., Phillips, M. M., & Terlevich, R. 1981, PASP, 93, 5
Banerji, M., Fabian, A., & McMahon, R. G. 2014, MNRAS, 439, L51
Barcos-Munoz, L., Leroy, A. J., Evans, A. S., et al. 2015, ApJ, 799, 10
Becker, R. H., White, R. L., & Helfand, D. J. 1995, ApJ, 450, 559
Bendo, G., Baes, M., Biancji, S., et al. 2015, MNRAS, 448, 135
Best, P. N., & Heckman, T. M. 2012, MNRAS, 421, 1569
Best, P. N., Ker, L. M., Simpson, C., Rigy, E. E., & Sabater, J. 2014, MNRAS, 445, 955
Bolatto, A. D., Wolfire, M., & Leroy, A. K. 2013, ARA&A, 51, 207
Bridge, C. R., Blain, A. W., Borys, C. J. K., et al. 2013, ApJ, 769, 91 (EWB12)
Carilii, C., & Walter, F. 2013, ARA&A, 51, 105
Cattaneo, A., & Teyssier, R. 2007, MNRAS, 376, 1547
Cleary, K., Lawrence, C. R., Marshall, J. A., Hao, L., & Meier, D. 2007, ASPC, 373, 475
Combes, F., Garcia-Burillo, S., Casaola, V., et al. 2013, A&A, 558, 124
Condon, J. J., Cotton, W. D., Greisen, E. W., et al. 1998, AJ, 115, 1693
Croton, C. 2006, MNRAS, 365, 11
Cutri, R., Wright, E. L., Conrow, T., et al. 2012, WISE Explanatory Supplement, http://wise2.ipac.caltech.edu/docs/release/allwise/expsup/index.html
Dallacasa, D., Stanghellini, C., Centonza, M., & Fanti, R. 2000, A&A, 363, 887
Dasyra, K. M., & Combes, F. 2012, A&A, 541, L7
Dasyra, K. M., Combes, F., Novak, G. S., et al. 2014, A&A, 565, 46
De Breuck, C., Seymour, N., Stern, D. J, et al. 2010, ApJ, 725, 36
Delvecchio, I., Lutz, D., Berta, S., et al. 2015, MNRAS, 449, 373
Dey, A., Soifer, B. T., Desai, V., et al. 2008, ApJ, 677, 943
De Young, D. 2010, ApJ, 710, 743
Dicken, D., Tadhunter, C., Axon, D., et al. 2011, ApJ, 741, 126
Dowell, C. D., Allen, C. A., Babu, R. S., et al. 2003, Proc. SPIE, 4855, 73
Downes, D., & Solomon, P. 1998, ApJ, 507, 615
Efstathiou, A. 2006, MNRAS, 371, L70
Efstathiou, A., Christopher, N., Verma, A., & Siebenmorgen, R. 2013, MNRAS, 436, 1873
Efstathiou, A., & Rowan-Robinson, M. 1995, MNRAS, 273, 649
Efstathiou, A., Rowan-Robinson, M., & Siebenmorgen, R. 2000, MNRAS, 313, 734
Efstathiou, A., & Siebenmorgen, R. 2009, A&A, 502, 541
Eisenhardt, P. R. M., Wu, J., Tsai, C.-W., et al. 2012, ApJ, 755, 173 (EWB12)
Elitzur, M. 2012, ApJL, 747, L33
Elvis, M., Wilkes, B. J., McDowell, J. C. R., et al. 1994, ApJS, 95, 1
Fabian, A. 2010, ARA&A, 50, 455
Farrah, D., Bernard-Salas, J., Spoon, H. W. W., et al. 2007, ApJ, 667, 149
Feruglio, C., Fiore, F., Carniani, S., et al. 2015, in press
Feruglio, C., Maiolino, R., Pinconcelli, E., et al. 2010, A&A, 518, L155
Fiolet, N., Omont, A., Polletta, M., et al. 2009, A&A, 508, 117
Fischer, J., Sturm, E., Gonzalez-Alfonso, E., et al. 2010, A&A, 518, L41
Fu, H., & Stockton, A. 2007, ApJ, 666, 794
Garca-Burillo, S., Combes, F., Usero, A., et al. 2014, A&A, 567, 125
Gonzalez-Alfonso, E., Fischer, J., Graci-Carpio, J., et al. 2014, A&A, 561, 27
Griffin, M. J., Abreu, A., Ade, P. A. R., et al. 2010, A&A, 518, L3
Grimes, J. A., Rawlings, S., & Willox, C. J. 2005, MNRAS, 359, 1345
Guillard, P., Boulanger, F., Lehnert, M. D., et al. 2015, A&A, 574, A32
Guillard, P., Ogle, P. M., Emonts, B. H. C., et al. 2012, ApJ, 747, 95
Heckman, T. M., & Best, P. N. 2014, ARA&A, 52, 589
Holt, J., Tadhunter, C. M., & Morganti, R. 2008, AN, 387, 639
Ibar, E., Cirasuolo, M., Ivison, R., et al. 2008, MNRAS, 386, 953
Ivison, R. J., Chapman, S. C., Faber, S. M., et al. 2007, ApJ, 660, 77
Jarrett, T. H., Cohen, M., Masci, F., et al. 2011, ApJ, 735, 112
Jones, S., Blain, A. W., Lonsdale, C. J., et al. 2015, MNRAS, 448, 3325
Jones, S. F., Blain, A. W., Stern, D., et al. 2014, MNRAS, 443, 146
Kennicutt, R. C. 1998, ApJ, 498, 181
Kewley, L. J., Maier, C., Yabe, K., et al. 2013, ApJ, 774, 10
Kim, M., Ho, L. C., Lonsdale, C. J., et al. 2013, ApJL, 768, L9
Kormendy, J., & Ho, L. C. 2013, ARA&A, 51, 511
Lacy, M., Petric, A. O., Martinez-Sansigre, A., et al. 2011, AJ, 142, 196
Lacy, M., Ridgway, S. E., Sajina, A., et al. 2015, ApJ, 802, 102
Lanz, L., Ogle, P. M., Evans, D., et al. 2015, ApJ, 801, 17
Leitherer, C., & Chen, J. 2010, NewA, 14, 356
Leroy, A. K., Walter, F., Bigiel, F., et al. 2009, AJ, 137, 4670
Lonsdale, C. J., Lonsdale, C. J., Smith, H. E., & Diamond, P. 2003, ApJ, 592, 804
Lonsdale, C. J., Polletta, M., Omont, A., et al. 2009, ApJ, 692, 422
Lonsdale, C. J., Polletta, M., Surace, J., et al. 2004, ApJS, 154, 54
Lutz, D., Yan, L., Armus, L., et al. 2005, ApJL, 632, L13
Magnelli, B., Lutz, D., Santini, P., et al. 2012, A&A, 539, 155
Maraston, C. 2005, MNRAS, 362, 799
Melbourne, J., Soifer, B. T., Desai, V., et al. 2012, AJ, 143, 125

Morganti, R., Frieswijk, W., Oonk, R. J. B., Oosterloo, T., & Tadhunter, C. 2013, A&A, 552, L4
Morganti, R., Tadhunter, C. N., Oosterloo, T. A., et al. 2003, PASA, 20, 129
Mullaney, J. R., Alexander, D. M., Fine, S., et al. 2013, MNRAS, 433, 622
Mullaney, J. R., Alexander, D. M., Goulding, A. D., & Hickox, R. C. 2011, MNRAS, 414, 1082
Nenkova, M., Sirocky, M. M., Ivezic, Z., & Elitzur, M. 2008, ApJ, 685, 147
Nesvadba, N., Lehnert, M., De Breuck, C., Gilbert, A., & van Breughel, W. 2008, A&A, 479, 67
Nesvadba, N. H., Boulanger, F., Lehnert, M. D., Guillard, P., & Salome, P. 2011a, A&A, 536, L5
Nesvadba, N. P. H., Polletta, M., Lehnert, M. D., et al. 2011b, MNRAS, 415, 2359
Netzer, H., Lutz, D., Schweitzer, M., et al. 2007, ApJ, 666, 806
O'Dea, C. 1998, PASP, 110, 493
Ogle, P., Boulanger, F., Guillard, P., et al. 2010, ApJ, 724, 1193
Pinconcelli, E., Vignali, C., Bianchi, S., et al. 2015, A&A, 574, 9
Poglitsch, A., Waelkens, C., Geis, N., et al. 2010, A&A, 518, 2
Polletta, M., Omont, A., Berta, S., et al. 2008, A&A, 492, 81
Polletta, M., Tajer, M., Maraschi, L., et al. 2007, ApJ, 663, 81
Polletta, M., Wilkes, B. J., Siana, B., et al. 2006, ApJ, 642, 673
Priddey, R. S., Gallagher, S. C., Isaak, K. G., et al. 2007, MNRAS, 374, 867
Priddey, R. S., Isaak, K. G., McMahon, R. G., Robson, E. I., & Pearson, C. P. 2003, MNRAS, 344, L74
Ramos-Almeida, C., Snchez-Portal, M., Prez Garca, A. M., et al. 2013, MNRAS, 417, 46
Richards, G. T., Lacy, M., Storrie-Lombardi, L. J., et al. 2006, ApJS, 166, 470
Sajina, A., Yan, L., Fadda, D., et al. 2012, ApJ, 757, 13
Scoville, N., Sheth, K., Walter, F., et al. 2015, ApJ, 800, 108
Scoville, N. Z., Aussel, H., Sheth, K. S., et al. 2014, ApJ, 783, 84
Seymour, N., Stern, D., De Breuck, C., et al. 2007, ApJS, 171, 353
Shang, Z., Brotherton, M. S., Wills, B. J., et al. 2011, ApJS, 196, 2
Shih, H.-Y., & Stockton, A. S. 2014, ApJ, 794, 117
Silva, A., Sajina, A., Lonsdale, C., & Lacy, M. 2015, ApJL, 806, L25
Simpson, C., Rawlings, S., Ivison, R., et al. 2012, MNRAS, 421, 3060
Stalevski, M., Fritz, J., Baes, M., Nakos, T., & Popovic, L. 2012, MNRAS, 420, 2756
Stern, D., Assef, R. J., Benford, D. J., et al. 2012, ApJ, 753, 30
Stern, D., Lansbury, G. B., Assef, R. J., et al. 2014, ApJ, 794, 102
Sturm, E., Gonzalez-Alfonso, E., Veilleux, S., et al. 2011, ApJ, 733, 16
Tadhunter, C., Dicken, D., Morganti, R., et al. 2014a, MNRAS, 445, 51
Tadhunter, C., Holt, J., Gonzalez Delgado, R., et al. 2011, MNRAS, 412, 960
Tadhunter, C., Morganti, R., Rose, M., Oonk, J. B. R., & Oosterloo, T. 2014b, Natur, 511, 440
Tsai, C.-W., Eisenhardt, P., Wu, J., et al. 2015, ApJ, 805, 90
Ulvestad, J. S., Wrobel, J. M., & Carilli, C. L. 1999, ApJ, 516, 127
Veilleux, S., Melendez, M., Sturm, E., et al. 2013, ApJ, 776, 27
Wagner, A., & Bicknell, G. 2011, ApJ, 728, 9
Wagner, A., Bicknell, G., & Umemura, M. 2012, ApJ, 757, 136
Wagner, A., Umemura, M., & Bicknell, G. 2013, ApJL, 763, L18
Wilson, C. D., Rangwala, N., Glenn, J., et al. 2014, ApJ, 789, 36
Wright, E. L., Eisnehardt, P., Mainzer, A. K., et al. 2010, AJ, 140, 1868
Wu, J., Bussmann, R. S., Tsai, C.-W., et al. 2014, ApJ, 793, 8
Wu, J. J., Tsai, C.-W., Sayers, J., et al. 2012, ApJ, 756, 96 (EWB12)
Yan, L., Chary, R., Armus, L., et al. 2005, ApJ, 628, 60
Yan, L., Donoso, E., Tsai, C.-W., et al. 2013, AJ, 145, 55
Zhang, K., Wang, T.-G., Yan, L., & Dong, X.-B. 2013, ApJ, 768, 22